

---

Electronic Theses and Dissertations, 2020-


---

2022

## Patterned Liquid Crystal Devices for Near-eye Displays

Kun Yin

*University of Central Florida*

 Part of the [Electromagnetics and Photonics Commons](#), and the [Optics Commons](#)  
Find similar works at: <https://stars.library.ucf.edu/etd2020>  
University of Central Florida Libraries <http://library.ucf.edu>

This Doctoral Dissertation (Open Access) is brought to you for free and open access by STARS. It has been accepted for inclusion in Electronic Theses and Dissertations, 2020- by an authorized administrator of STARS. For more information, please contact [STARS@ucf.edu](mailto:STARS@ucf.edu).

---

### STARS Citation

Yin, Kun, "Patterned Liquid Crystal Devices for Near-eye Displays" (2022). *Electronic Theses and Dissertations, 2020-*. 1118.

<https://stars.library.ucf.edu/etd2020/1118>

PATTERNED LIQUID CRYSTAL DEVICES FOR NEAR-EYE DISPLAYS

by

KUN YIN  
B.S. Tianjin University, 2016

A dissertation submitted in partial fulfillment of the requirements  
for the degree of Doctor of Philosophy  
in the College of Optics and Photonics  
at the University of Central Florida  
Orlando, Florida

Spring Term  
2022

Major Professor: Shin-Tson Wu

© 2022 Kun Yin

## ABSTRACT

As a promising next-generation display, augmented reality (AR) and virtual reality (VR) have shown attractive features and attracted broad interests from both academia and industry. Currently, these near-eye displays (NEDs) have enabled numerous applications, ranging from education, medical, entertainment, to engineering, with the help of compact and functional patterned liquid crystal (LC) devices. The interplay between LC patterns and NEDs stimulates the development of novel LC devices with unique surface alignments and volume structures, which in turn feedback to achieve more compact and versatile NEDs.

This dissertation will focus on the patterned LC with applications in NEDs. Firstly, we propose and explain the working principles and generation of novel patterned LC devices, including LC configurations, surface alignment mechanism, polarization field generation, and fabrication process. Secondly, we theoretically analyze the optical properties of patterned LC devices, providing the optical efficiency, devices thickness, polarization selectivity, wavelength, and angular bandwidth. Based on the dimensions of the surface pattern, the LC devices can be divided into reflector, grating, and lens, respectively. Finally, we focus on the applications of these novel patterned LC devices to address some challenges in current NEDs.

More specifically, achieving a high-resolution density in NEDs, especially for VR systems is an urgent issue. To enhance the resolution without introducing any extra burden to the system, we propose an elegant method with the combination of foveated view and polarization multiplexing, based on LC reflector. For LC grating, it shows a nearly 100% efficiency with a large diffraction angle, which is a perfect candidate for the waveguide-based AR systems. We propose and demonstrate the LC grating-based waveguide AR with benchtop demo and further

performance optimization. For LC lens, it can achieve controllable power and large off-axis angle while maintaining high efficiency. These unique and attractive features give LC lenses the ability to achieve a glasses-like AR architecture while maintaining high optical efficiency. Based on this LC lens, we demonstrate a novel AR system design using polarization and time multiplexing methods to simultaneously obtain a double field of view and a glasses-like form factor.

The proposed patterned LC devices for NED applications are validated by both optical simulation and experiment. Multiple tabletop demos are constructed to illustrate how these patterned LC devices can significantly improve the visual experiences of these next-generation NEDs.

To my family.

## ACKNOWLEDGMENTS

Ph.D. study is a challenging yet exciting and interesting experience. I am extremely grateful for all the support I received during my time at CREOL, without which I would not be able to enjoy this great journey.

First and foremost, I would like to express my deepest appreciation to my advisor, Dr. Shin-Tson Wu. With full support and patience, he led me on my Ph.D. study. What I learned from him was not only how to be a good researcher, but also how to be a better person. "Do the right thing in the right way." "Speak the truth in love." These guidelines will affect me for my entire life. Furthermore, his visionary leadership, patient mentoring, and constant encouragement have been a source of self-motivation throughout my graduate work, allowing me to fearlessly explore new and meaningful techniques. Besides, I would also like to thank his better half, Cho-Yan Hsieh, for her warm love and care over the past years.

I would like to thank my committee members, Prof. Jim Moharam, Prof. Patrick L. LiKamWa, and Prof. Yajie Dong. They have been providing inspiring discussions and constructive feedback on this dissertation and making strong recommendations for my society award and scholarship applications without hesitation.

I would like to thank all these kind, smart, and talented people I met and worked with during my Ph.D. study, especially Yan Li, Linghui Rao, Fenglin Peng, Ruidong Zhu, GuanJun Tan, Juan He, Fangwang Gou, Yuge Huang, Ziqian He, Jianghao Xiong, Md Javed Rouf Talukder, Yannanqi Li, En-Lin Hsiang, Junyu Zou, Zhiyong Yang, Qian Yang, Zhenyi Luo, Yizhou Qian, Hao Chen, and Caicai Zhang. Special thanks to Yun-Han Lee for introducing me to LC research, Lab course 101, and continuously supporting me with interesting discussions and fruitful

collaborations. I also sincerely appreciate the help and support from Haiwei Chen during my job interview.

Last but not least, I would like to express my deepest gratitude to my parents for their everlasting and unconditional love, support, and encouragement throughout my academic endeavors.



## TABLE OF CONTENTS

LIST OF FIGURES .....	x
LIST OF TABLES .....	xiv
CHAPTER 1 : INTRODUCTION .....	1
CHAPTER 2 : LC DEVICES ENABLED BY TWO-PHOTON POLYMERIZATION .....	5
2.1 Background .....	5
2.2 Optical properties .....	8
2.3 Fabrication Methods .....	19
2.4 Summary .....	22
CHAPTER 3 : FOVEATED IMAGING VR ENABLED BY CLC REFLECTOR.....	23
3.1 Background .....	23
3.2 System Design .....	24
3.3 System Integration .....	28
3.4 Summary .....	34
CHAPTER 4 : WAVEGUIDE AR ENABLED BY PVG .....	35
4.1 Background .....	35
4.2 Achieving CPVGs.....	37
4.3 CPVG Fabrication.....	42
4.4 Multilayer PVG.....	44
4.5 System Integration .....	49
4.6 Summary .....	52

CHAPTER 5 : GLASSES-LIKE AR ENABLED BY PVL .....	35
5.1 Background .....	54
5.2 Polarizaion Multiplexing .....	57
5.3 Experiments .....	62
5.4 Summary .....	70
CHAPTER 6 : CONCLUSIONS .....	54
APPENDIX: STUDENT PUBLICATIONS.....	74
REFERENCES .....	81

## LIST OF FIGURES

Figure 1-1 Illustration of the relationship between patterned LC devices and NEDs. ....	3
Figure 2-1 Schematic illustration of patterned cholesteric LC devices: (a) a reflector, (b) a grating, and (c) a lens. ....	7
Figure 2-2 Different LC director configurations of PVG. (a) Planar-PVG with helical axis perpendicular to substrate surface. (b) Slanted-PVG with helical axis perpendicular to Bragg surface. The red box indicates the transitional region from planar to slanted structure. ....	10
Figure 2-3 Simulated diffraction efficiency as a function of film thickness. ....	11
Figure 2-4 Wavelength response of PVGs. (a) Diffraction efficiency spectra with different refractive index contrast and (b) different diffraction angles. ....	13
Figure 2-5 Angular response of PVGs. (a) Diffraction efficiency spectra with different incident angle and (b) different diffraction angles.....	14
Figure 2-6 Stokes parameters S3 as a function of film thickness.....	15
Figure 2-7 Schematic of the beam focus formed by an PVL and the detailed LC director orientation inside the PVL.....	17
Figure 2-8 The simulated diffractive phase of a 20 mm × 20 mm PVL.....	18
Figure 2-9 Fabrication procedures of PVGs. (a) Surface alignment for LC polymeric PVG. (b) Electrically responsive LC PVG. (c) Volume alignment.....	19
Figure 2-10 Exposure setups of CLC devices. (a) CLC reflector exposure. (b) Two-beams interferometer for PVG and PVL. (b) Exposure based on phase pattern generated by SLM.....	21
Figure 3-1 Schematic diagram of the proposed multi-resolution foveated display for a VR headset. DM: Display module; HM: Half mirror; CLC: Cholesteric liquid crystal. ....	25

Figure 3-2 The unfolded layout of the optical paths for (a) peripheral image with low resolution, and (b) center image with high resolution. ....	26
Figure 3-3 Schematic diagram of the proposed polarization multiplexed display module, including a display panel (DM), a polarization modulator, and a broadband quarter-wave plate (QWP). ..	27
Figure 3-4 Schematic illustration of the three-layer cholesteric LC reflector. ....	29
Figure 3-5 The displayed image: (a) peripheral image, (b) enlarged center image, and (c) combined image on the display panel.....	31
Figure 3-6 Picture of the benchtop demo and optical elements used in the system. ....	32
Figure 3-7 Experimental photographs of the proposed multi-resolution display with 4.4x resolution enhancement: (a) whole displayed image; (b) the magnified green square region in (a); (c) the magnified blue rectangle region in (b); (d) the magnified red rectangle region in (b).. ....	33
Figure 4-1 Illustration of waveguide AR with PVGs as input and output couplers. ....	36
Figure 4-2 LC director profile of the uniform PVG and CPVG. (a) The horizontal period is $P_x$ , the vertical period is $P_y$ , and the Bragg period is $P_B$ . (b) The horizontal periodicity is $P_x$ , the vertical periodicities are $P_{y1}$ and $P_{y2}$ at the bottom and top, respectively, and the Bragg period are $P_{B1}$ and $P_{B2}$ at the bottom and top, respectively.....	38
Figure 4-3 Simulated first-order diffraction efficiency. Angular response at $\lambda = 532$ nm of both gradient pitch CPVGs (blue line) and uniform pitch PVG (black line).....	40
Figure 4-4 (a) Simulated angular and spectral responses of the CPVGs. The black line shows the $\lambda=532$ nm. (b) The two-dimensional angular response of gradient-pitch PVG.....	41

Figure 4-5 The CPVG sample viewed from an oblique angle with the CPVG region circled by a blue line. (b) A photo taken through the CPVG sample, where the CPVG region is circled by a blue line. The distance between PVG and camera is 1 cm, and the target is 10 cm away. ....	43
Figure 4-6 Angular behavior of optical efficiency. ....	44
Figure 4-7 LC director profile of a multi-layer PVG. (b) Two-layer PVG. ....	45
Figure 4-8 Simulated and measured angular behavior of two-layer PVG. ....	47
Figure 4-9 Simulated first-order diffraction efficiency and angular response at $\lambda = 532$ nm of uniform PVG (red line), two-layer PVG (black line), and three-layer PVG (blue line).....	47
Figure 4-10 (a) Top view of a simplified AR module. (b) Photo of an AR module with a green laser diode input light.....	479
Figure 4-11 Picture of an AR prototype, including a micro-OLED panel and two CPVGs.....	47
Figure 4-12 Photo of the output image. ....	47
Figure 5-1 Illustration of a glasses-like AR with LCoS projector .....	47
Figure 5-2 Schematic illustrations of (a) a PVL with (b) surface alignment and (c) CLC structure. (d) Schematic diagram of the PDC with two combined PVLs. ....	47
Figure 5-3 Schematic illustrations of a polarization-time multiplexing free space AR system. ..	47
Figure 5-4 (a) PVL fabrication workflow. (b) Exposure setup.....	47
Figure 5-5 Photo of (a) the fabricated PVL-L and (b) the PDC consisting of PVL-L and PVL-R. (c) A photo taken through the PDC sample, where the PDC region is yellowish. ....	47
Figure 5-6 Schematic illustration of the experiment setup. ....	47
Figure 5-7 (a) Captured image of LCP light, UCF. (b) Captured image of RCP, school logo. (c) Captured image of the combined images.....	47

Figure 5-8 Schematic illustration of full-color system design with color wheel..... 47

Figure 5-9 Schematic illustrations of (a) an improved polarization-time multiplexing AR system with (b) a PDC composed of active HWP and PVLs. (c) Schematic illustrations of the image from each PVL..... 47

**LIST OF TABLES**

Table 4-1 Composition of the solutions (by weight). ..... 50

## CHAPTER 1 : INTRODUCTION

As a promising next-generation display, augmented reality (AR) and virtual reality (VR) provide an attractive new way for people to perceive the world [1,2]. Unlike conventional display technologies, such as computers and smartphones that place a panel in front of the viewer, near-eye displays (NEDs) are designed to revolutionize the interactions between the viewer, display, and surrounding environment. As an important information acquisition medium, NEDs bridge the gap between computer-generated (CG) images and the real world [3]. On the one hand, VR displays generate a fully immersive virtual environment based on CG images, which has a sufficient field of view (FoV) to provide a refreshing virtual experience without relying on the viewer's real environment. On the other hand, AR displays offer see-through capability with an enriched surrounding environment. By overlapping virtual images with the real world, viewers can immerse in an imaginative world that combines fiction and reality.

Although some commercial NEDs have emerged in recent years, the origin of this technology can be traced back to the last century [3,4]. With the introduction of head-mounted display with virtual environment in the 1960s [4,5], such a novel display concept was once considered state-of-the-art. However, due to the lack of flat panel displays, image rendering capabilities, related sensors, wireless data transfer, and well-designed optical components, this display technology, which was ahead of its time then, came to an end. Fortunately, with the rapid development of optics [6-8], high-resolution displays [9], and information technologies [10] in recent years, AR and VR are blooming again. Because of the impressive visual experience and high degrees of interaction between viewers and CG images, AR and VR are promising for



widespread applications, including, but not limited to, healthcare, education, engineering design, manufacturing, and entertainment [1,2].

The goals of AR and VR displays are to provide reality-like clear images that can simulate, merge into, or rebuild the surrounding environment without wearer discomfort [11,12]. Specifically, visual comfort has to meet the requirements of the human visual system based on the eye-to-brain imaging process, otherwise, the viewer will feel unreal, unclear, or even dizzy and nauseous. Usually, the human eye has a large FoV: about  $160^\circ$  in the horizontal and  $130^\circ$  in the vertical directions for each eye (monocular vision). The overlapped binocular vision still has  $120^\circ$  FoV in the horizontal direction [13]. In parallel, the diopter and rotation of the human eye lens can collaborate to focus on different positions of a real object with the correct depth of field and blur the other portions [14]. Therefore, to achieve visual comfort, the optical system should provide an adequate FoV, high resolution, and offer sufficient contrast and brightness. It is worth mentioning that the above requirements are preliminary. To further optimize the system and provide a high-quality experience that meets different scenarios, we also need 3D imaging, occlusion, and full-color without aberrations, to name just a few examples.

Therefore, integrating these specific requirements into near-eye devices is a huge challenge to the size, quality, and optical properties of conventional optical elements such as refractive lenses, beam splitter cubes, prism couplers, etc.

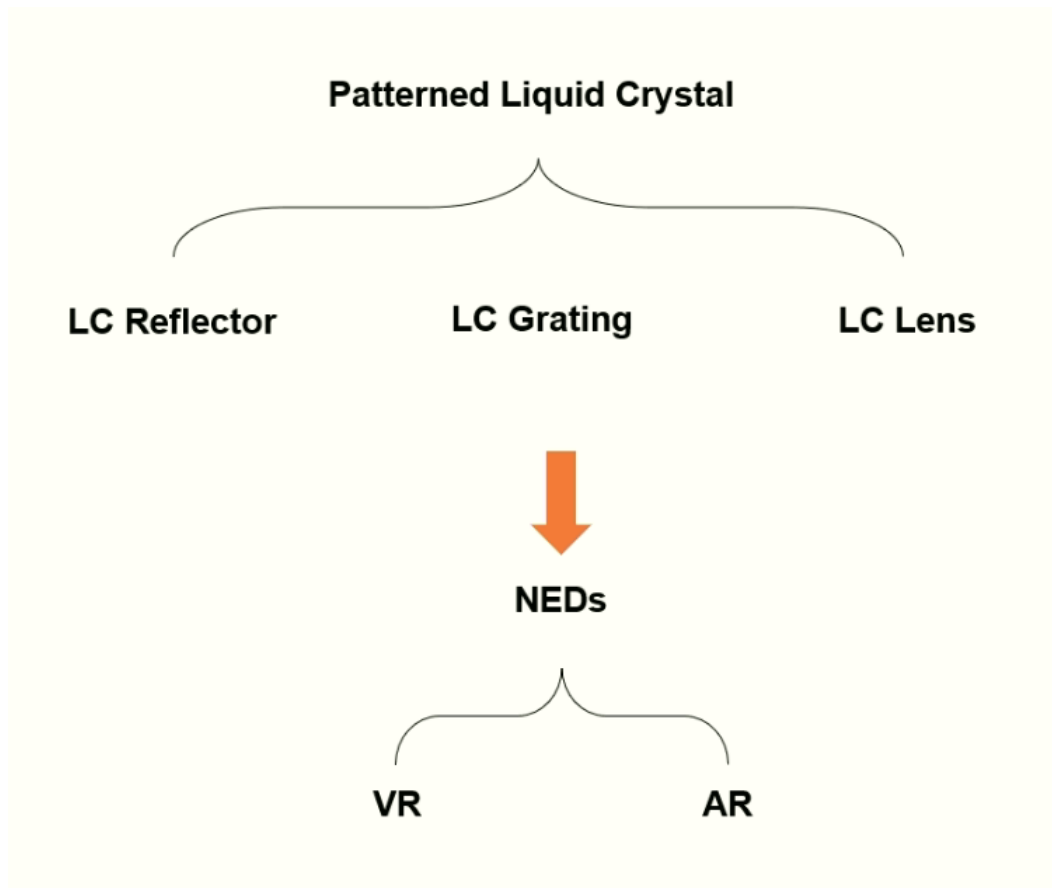


**Figure 1-1: Illustration of the relationship between patterned LC devices and NEDs.**

Lately, patterned LC optical devices [15-19] have attracted increasing interest due to their advantages in nearly 100% efficiency, polarization selectivity, large optical power, low cost, and thin form factor. These patterned LC devices with several micrometers thickness enable compact and lightweight optical components. By controlling the surface patterns of these LC devices, various modulation capabilities can be obtained without sacrificing the advantages of the thin form factor. These unique patterned LC devices can be employed to address the major challenges or meet the challenging requirements in NEDs.

In addition, the applications of NEDs also feedback the development of patterned LC devices. Tremendous efforts from both academia and industry attract more interest from

worldwide, leading to the bloom of patterned LC devices with various functions and impressive optical performance. [Figure 1](#) briefly illustrates the relationship between LC patterned devices and NEDs.

In this dissertation, both patterned LC devices and the applications in NEDs are fully presented. In Chapter Two, the working principle and unique features of the patterned LC devices are introduced, including LC configurations, optical responses, and fabrication processes. Next, we discuss three advanced near-eye system designs based on different patterned liquid crystal devices. In Chapter Three, a polarization-multiplexed foveated imaging system using LC reflector is presented to enhance the angular resolution of VR display 4.4 times. Chapter Four describes a waveguide-guide AR system based on our homemade LC gratings, which is able to achieve high efficiency and large FoV. Chapter Five discusses a novel optical design for glasses-like AR NEDs, where LC lens-based polarization-dependent combiner is designed and integrated with a projection-type AR system such that the FoV can be doubled with a compact form factor. Chapter six provides a summary and conclusion.

## CHAPTER 2 : PATTERNED LC DEVICES

### 2.1 Background

Different from conventional refractive optics that use the optical path difference to produce phase, patterned LC devices generate the desired phase profile by spatially varying the LC orientations, which is controlled through the alignment patterning on the bottom surface [20,21]. By generating the desired patterns and corresponding LC volume structures, distinct optical properties, such as a flat surface, ultrathin form factor, high diffraction efficiency, strong polarization dependency, tunable bandwidth, and high optical quality can be achieved. The basic working principle of these patterned LC devices is the modulation of the LC material's refractive index, which is established and controlled by the surface alignment and the self-organization of LC molecules.

Based on the abovementioned principle, an arbitrary phase pattern can be achieved by patterning the LC or LC polymer on a flat surface. Although various types of patterned LC devices with both transmissive type and reflective type have been demonstrated, including reflectors [22], deflectors [17,18], lenses [23,24], axicons [25], and q-plates [26-28], the reflective type of LC devices are of more interest in NED applications due to the single first order with nearly 100% efficiency, enabling large optical power, folded optical path with more compact form factor. These reflective patterned LC devices, based on the Bragg-Berry phase [29], are mainly made of cholesteric LCs (CLCs) and work under Bragg condition, enabling tunable spectral bandwidth and angular responses. A typical CLC device can realize liquid crystalline phase by self-organized molecules to form helical structure. If the circularly polarized light (e.g., left-handed circularly polarized (LCP)) has the same handedness as the helical twist, the light propagating along the

helical axis will experience Bragg reflection at normal incidence over the spectral range  $2n_o\Lambda_B < \lambda < 2n_e\Lambda_B$ , where  $\Lambda_B$  is the chiral period, and  $n_o$  and  $n_e$  are the ordinary and extraordinary refractive indices. The component with opposite circular polarization (e.g., right-handed circularly polarized (RCP)) will pass through the liquid crystal layer without any change.

Based on the dimension of the patterns, the CLC devices can be categorized into three main parts:

- (1) zero-dimension with homogeneous alignment for CLC reflector [29].
- (2) one-dimension with linear change alignment for CLC grating [30].
- (3) two-dimension with parabolic change alignment for CLC lens [24].

[Figure 2-1\(a\)](#) displays the optical response in a CLC reflector with the homogeneous pattern that makes the Bragg surface be parallel to the horizontal axis, thus performing like a mirror but with some distinct features. This unique CLC reflects the circularly polarized light (e.g., LCP) within one band having the same handedness as the cholesteric helix, whereas transmitting the circularly polarized light (e.g., RCP) with opposite handedness. [Figure 2-1\(b\)](#) shows a CLC grating with a large diffraction angle. Due to the polarization selectivity, the LCP light is diffracted, and the opposite polarization light transmits the grating without changing the polarization state and propagation direction. As a kind of Bragg volume gratings, this CLC grating with Bragg surfaces is also known as polarization volume grating (PVG). [Figure 2-1\(c\)](#) shows a CLC lens with a parabolic phase pattern. This CLC lens with off-axis angle and large optical power is also known as polarization volume lens (PVL). The LCP light will be diffracted and focused while the RCP light will just transmit without any change.

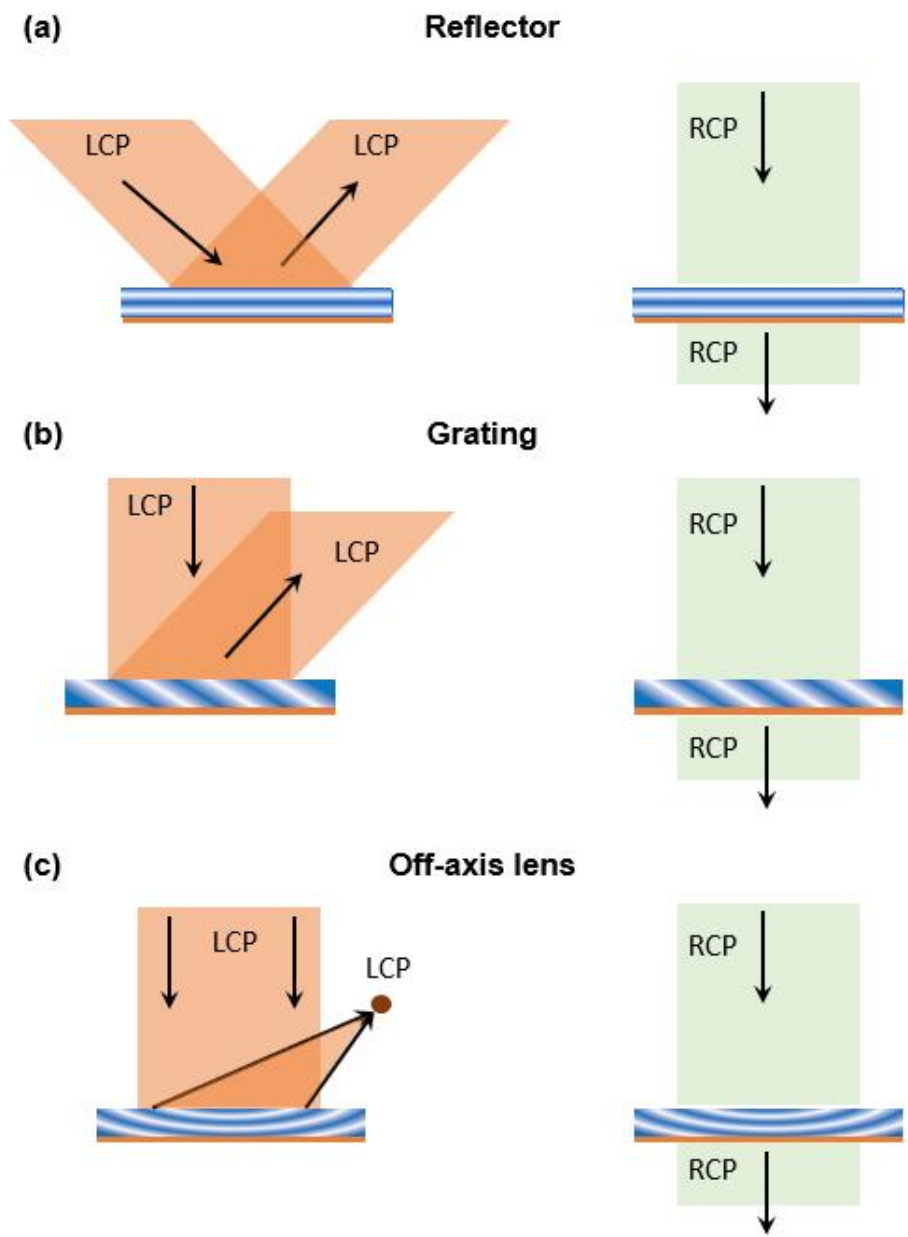


**Figure 2-1 Schematic illustration of patterned cholesteric LC devices: (a) a reflector, (b) a grating, and (c) a lens.**

## 2.2 Optical Properties

The CLC reflector is based on a homogeneous pattern. It can be simply treated as the reflection of Bragg surfaces. The PVL can be treated as a combination of many PVGs with different directions. Therefore, to fully understand patterned CLC devices, the most important is the configuration of CLC grating. Before we dive into the physical principles, we need to know the internal structure of CLC grating. Interestingly, with further research on physical models and experiments, the understanding of the LC director configuration in PVGs has experienced a transition. At first, the bulk structure was thought to be planar as Fig. 2-2(a) depicts, where all the LC directors are parallel to the substrate [30,31]. The helical axis of CLC is perpendicular to the substrate and the CLC structure rotates following the bottom sinusoidal alignment pattern. This configuration produces an overall Bragg structure with Bragg pitch obeying the following equation:

$$1/P_G^2 = 1/P_x^2 + 1/P_z^2, \quad (2-1)$$

where  $P_z$ , in this case, is the CLC pitch,  $P_x$  is the grating period, and  $P_G$  is the Bragg pitch. This presumed planar structure accords with our intuition in that all the LC directors follow the bottom planar alignment perfectly. Besides, like the geometric phase in transmissive LC polarization gratings [19,32], it also exists in reflective cholesteric LC structures [33]. The rotation of the helical axis, therefore, generates the geometric phase that can be utilized to fabricate various optical elements. So far, the planar structure explains some experimental results well. Nonetheless, it must be pointed out [34] that the bulk structure in planar-PVGs is not in the most relaxed state (pure helix structure), which is reflected in its free energy density (single-constant approximation).

Recently, some experiments on the polarization response in PVG indicate that the bulk structure may be in a slanted configuration [35]. This issue is explicitly explained in [34] through

simulation and experimental validation. The slanted PVG, as shown in Fig. 2-2(b), preserves the perfect helical structure in the bulk, which results in its lowest free energy (the bulk free energy is zero). The Bragg pitch  $P_G$  in this case is equal to the CLC pitch. The bottom alignment gives the bulk helical structure a tilt angle to match the bottom k-vector with the bulk periodic structure. To transit from the bottom planar alignment to the bulk slanted structure, there exists a transitional region (red box in Fig. 2-2(b)) with non-zero free energy. However, the thickness of this transitional region is usually very small (tens of nanometers), so its contribution to the total free energy is minor. As discussed in [36], the formation of planar-PVGs requires:

- (1) large  $P_x$  (where planar-PVGs and slanted-PVGs are indistinguishable).
- (2) strong anchoring and small thickness (less than 300 nm for each layer, and multiple spin-coatings to gain sufficient thickness, about 3  $\mu\text{m}$ ).

At the same time, except for polarization selectivity (which we will discuss later), the optical properties of planar-PVGs and slanted-PVGs are very similar in terms of reflection efficiency, wavelength response, and angular response. Therefore, from the perspective of practical application, the slanted-PVGs formed by one-time assembly are more advantageous. For the convenience of discussion, unless otherwise mentioned, the PVGs we refer to is the slanted ones.



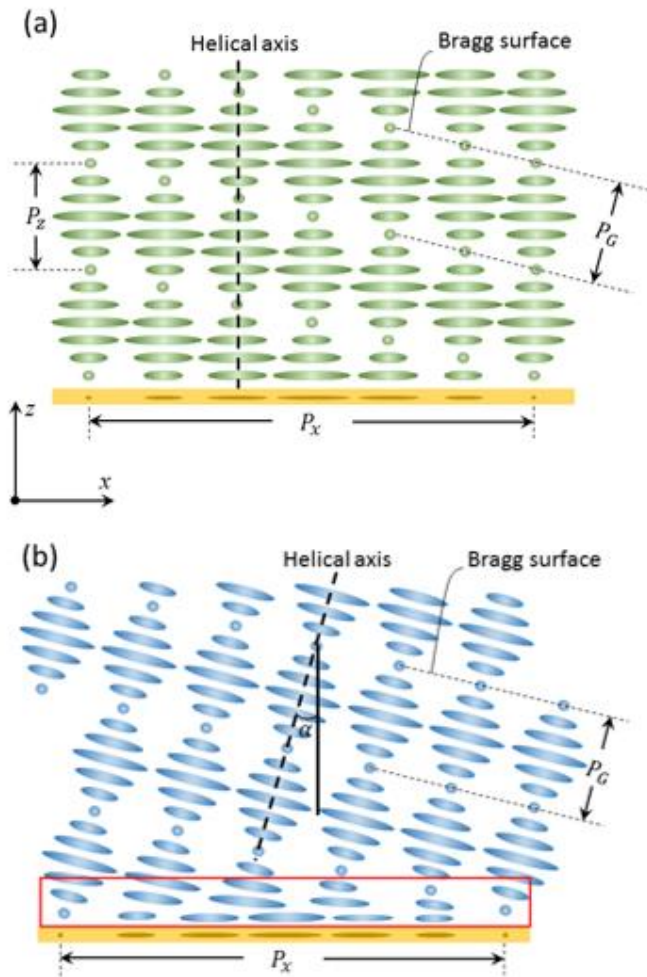


**Figure 2-2 Different LC director configurations of PVG. (a) Planar-PVG with helical axis perpendicular to substrate surface. (b) Slanted-PVG with helical axis perpendicular to Bragg surface. The red box indicates the transitional region from planar to slanted structure.**

To comprehensively show the diffractive properties of PVGs, we have built a rigorous model by using the commercialized Finite Element Method (FEM) package. For PVGs, there are several important characteristics that deserve special attention, including diffraction efficiency, wavelength response, angular response, and polarization response. Besides, as Bragg volume gratings, the PVGs should be thick enough to establish Bragg diffraction. As depicted in Fig. 2-3, the diffraction efficiency is directly related to the film thickness. The diffraction efficiency is

defined as the ratio of first-order diffracted light to incident light at a specific diffraction angle and center wavelength. The horizontal period is 440 nm, vertical period is 205 nm,  $\Delta n=0.15$ , the diffraction angle is  $50^\circ$ , and the central wavelength is 532 nm. The efficiency is higher than 95% when the thickness is 3  $\mu\text{m}$  with different resonance wavelengths. As the thickness increases, diffraction efficiency grows monotonically at the beginning and then gradually saturates and approaches 100%. Therefore, for a certain wavelength, the required thickness for achieving high diffraction efficiency can be easily obtained based on the number of pitches. Compared to a conventional volume holographic grating whose thickness is at least tens of micrometers, PVG (several micrometers) is much thinner. Besides, it is important to note that the efficiency is only for a circularly polarized input and the opposite circular polarization can fully transmit through the PVG. This feature provides high transmittance for the ambient light, which is important for see-through NEDs.

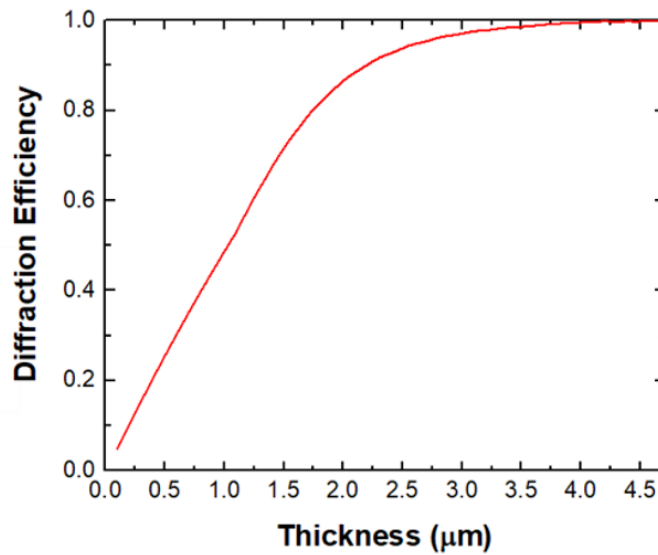


**Figure 2-3 Simulated diffraction efficiency as a function of film thickness.**

The effective index modulation in PVGs is essentially the birefringence of the LC material. Due to the matured LCD industry, a wide range of birefringence ( $\Delta n=0.05$  to  $0.4$ ) is available. Same as the spectral properties of CLC, the reflection band of PVGs could be easily tuned by using a LC with different  $\Delta n$ , as Fig. 2-4(a) depicts. Usually, as  $\Delta n$  increases, the reflection band gets wider. Figure 2-4(b) shows the diffraction efficiency spectra at three different diffraction angles with  $\Delta n$  of  $0.15$ .

From these simulation results, we can see that

- (1) The bandwidth of PVG can be precisely controlled by applying different LC materials with different  $\Delta n$ .
- (2) PVG can achieve a large diffraction angle ( $60^\circ$ ) while keeping high diffraction efficiency. Usually, the transmissive LC thin grating can only achieve  $\sim 5^\circ$  diffraction angle with high efficiency.
- (3) The diffraction efficiency and bandwidth are almost independent of the diffraction angle.

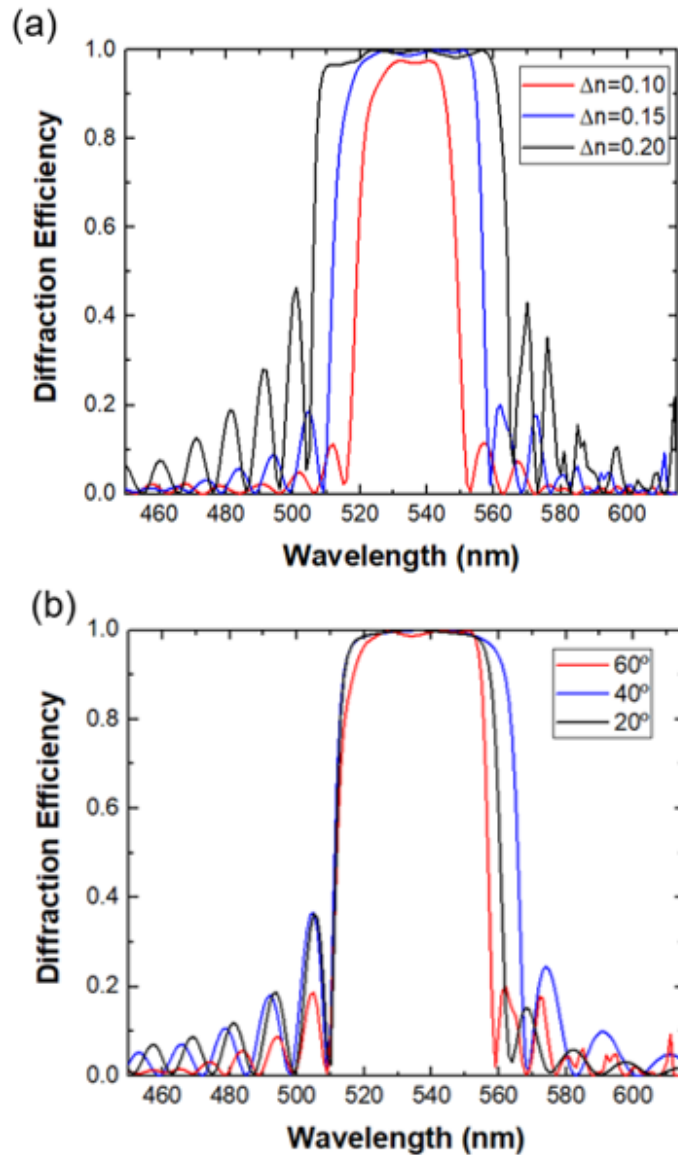


**Figure 2-4 Wavelength response of PVGs. (a) Diffraction efficiency spectra with different refractive index contrast and (b) different diffraction angles.**

Not only diffraction spectra, but the angular selectivity is also closely related to birefringence. Thus, the angular response via different birefringence is investigated and illustrated in Fig. 2-5(a). The angular band of incident light becomes broader as birefringence increases. Compared to the effective index modulation in holographic volume grating, the LC birefringence

is much higher. As a result, the PVGs possess wider angular bandwidth, which is much needed in NED systems. These will be discussed later. Besides, it is worth mentioning that the angular response is sensitive to diffraction angle as well. Figure 2-5(b) shows the angular bandwidth for different diffraction angles with the same  $\Delta n$ . The trend is clear: as the diffraction angle decreases, the angular band of incident light for achieving high diffraction efficiency is broader.

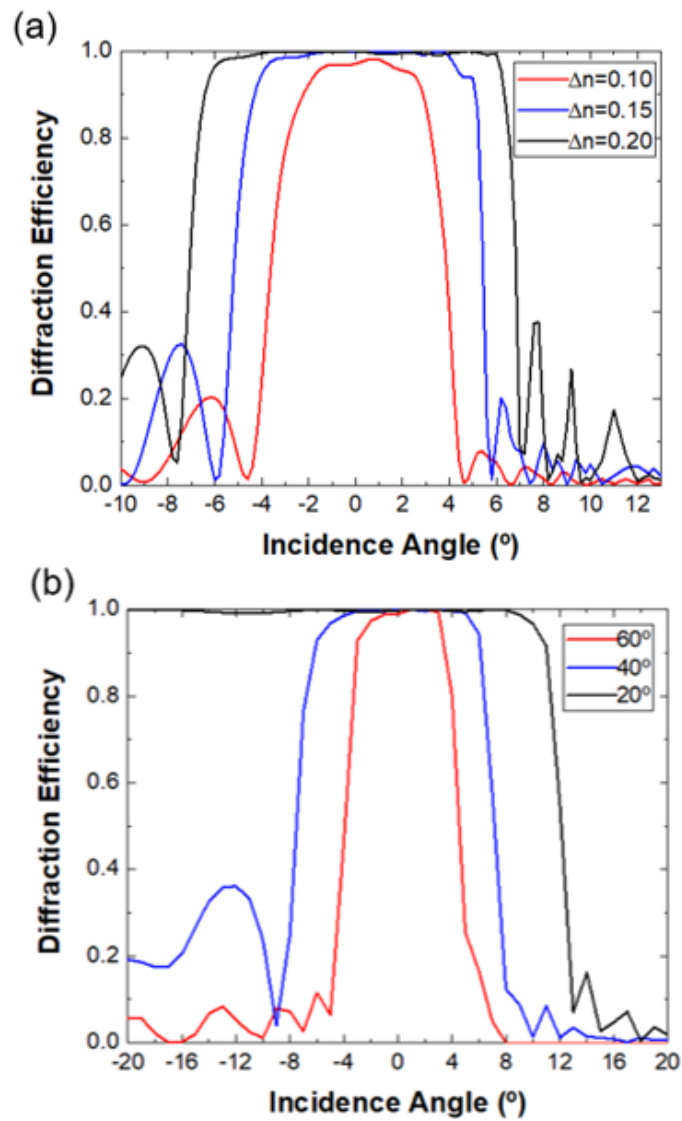


**Figure 2-5 Angular response of PVGs. (a) Diffraction efficiency spectra with different incident angle and (b) different diffraction angles.**

In addition to spectral and angular responses of PVGs, polarization response is another unique property. This part is rarely discussed in previous reports, but the study of the polarization properties is necessary for PVGs to be used in cascaded optical systems where polarization control is pivotal. In an early study, it was described that the first order diffracted light maintains a circular polarization with an appropriate input circular polarization [30]. Specifically, the input circularly polarized light will keep its handedness or flip its handedness when diffracted by a reflective or transmissive PVGs. To explain this, the slanted configuration of PVG was proposed. To investigate the polarization property of the diffracted light, we use Stokes parameter  $S_3$  as an indicator.  $S_3$  denotes the degree of circular polarization of light. For example,  $S_3=1$  means RCP light, while  $S_3=-1$  stands for LCP light. As Fig. 2-6 shows, the first order polarization state of the slanted configuration is very close to circular polarization. By contrast, the diffracted light from the planar PVG significantly deviates from the circular polarization.

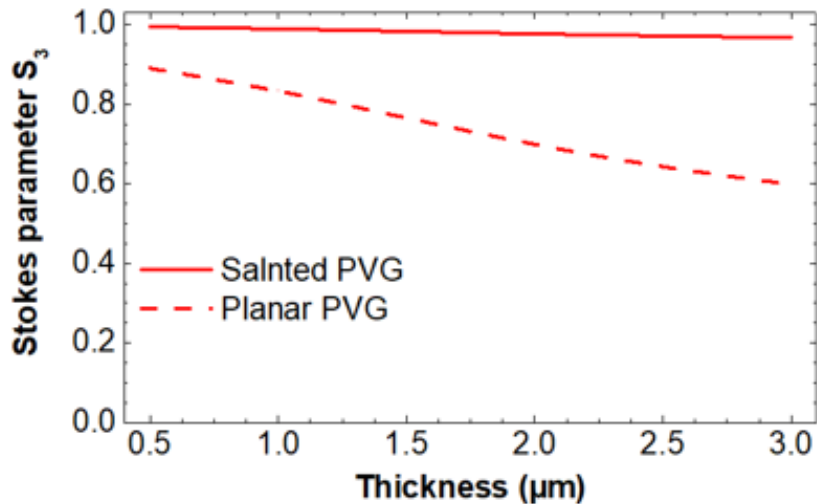


**Figure 2-6 Stokes parameters  $S_3$  as a function of film thickness.**

As we mentioned previously, PVL can be treated as a combination of PVGs with different periods and directions. [Figure 2-7](#) illustrates the LC configuration of a PVL. Similar to PVG, the substrate of PVL is treated to provide a rotation of LC optical axis in  $x$ -plane. The difference is for PVL, the rotation and the alignment supported by the substrate is not only in  $x$ -plane but also in  $y$ -plane. The rotating angle changes continuously and periodically to generate a lens-phase profile in the  $xy$ -plane.

When examining the detailed structure inside this device, the CLCs are precisely aligned in the horizontal plane and twisted in vertical direction along a slanted helical axis. At a macroscopic level, the PVL has a parabolic phase profile, but when we zoom into a small area, the LC structure works as a PVG with a linear phase profile. For a circularly polarized incident light (LCP or RCP) with the same handedness as the helical twist, the reflected beam from the PVL is converged at an off-axis angle without changing its polarization state. The operation principle is equivalent to combining a PVG with a convex lens for use as an off-axis concave mirror: the incident light is converged by the lens profile and diffracted by the grating, thereby forming such a reflective off-axis focus [24]. The diffraction efficiency of each small area, angular response, and wavelength response can also refer to the PVG simulation results.

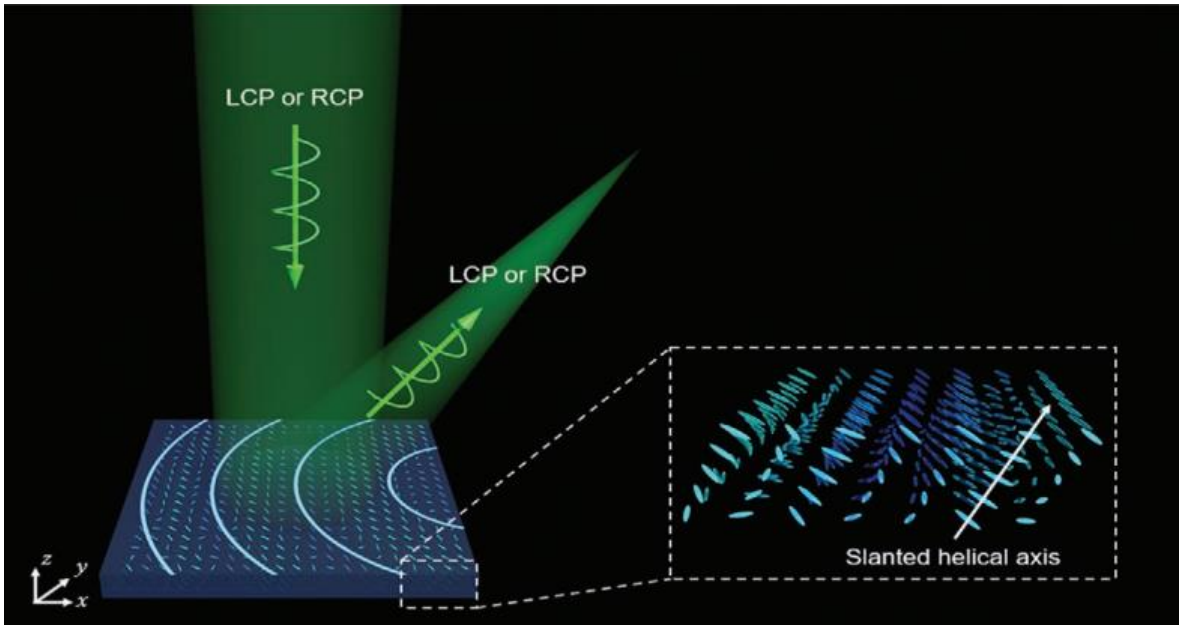


**Figure 2-7 Schematic of the beam focus formed by an PVL and the detailed LC director orientation inside the PVL.**

To intuitively understand the phase profile of this off-axis lens, we plot the phase of the diffracted light in Fig. 2-8. The size is set to be  $20 \text{ mm} \times 20 \text{ mm}$ . The diffracted phase is supposed to change from  $0$  to  $2\pi$ , however, the period is only several nanometers, which is too small to be observed in the range of  $20 \text{ mm}$ . Therefore, the phase is the accumulated phase, from  $0$  to  $2\pi$ , and then from  $2\pi$  to  $4\pi$ , and so on.



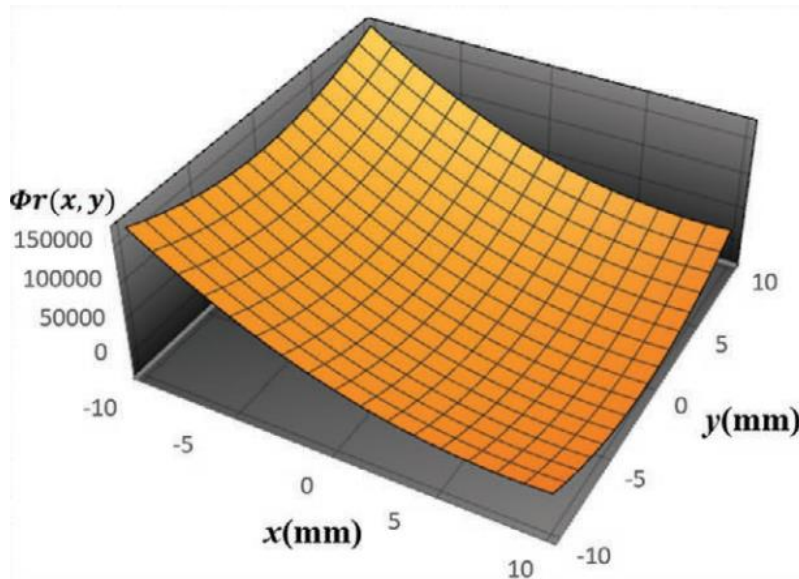


**Figure 2-8** The simulated diffractive phase of a 20 mm × 20 mm PVL.

### 2.3 Fabrication Methods

In addition to unique optical characteristics, the simple fabrication process is another noteworthy advantage of patterned CLC devices. Since the pattern will determine the function of the devices, recording high-quality patterns to align LC molecules is an important step during fabrication. Compared to the conventional rubbing method [37], photo-alignment is a more advantageous option for generating controllable and precise patterns [38-39].

Two approaches have been widely used in the fabrication based on photo-alignment materials. The first approach is surface alignment, which utilizes polarization interference to pattern a thin photo-alignment layer (PAL) [40-44]. The subsequently coated or sprayed liquid crystals self-align into volume structure following the recorded patterned surface. To fabricate a polymeric CLC film, the LC precursor typically contains LC monomer, chiral dopant, solvent, photo-initiator, and surfactant [45,46]. After the alignment process, we expose the sample with ultra-violet light to polymerize the film. By the contrast, to fabricate an electrically switchable

CLC device, two thin PAL-coated glass substrates are assembled to form a uniform cell. After recording the alignment, we inject LC material to the cell at an isotropic phase temperature [47] and let it cool down to the room temperature. Then the optical behavior of the CLC device can be tuned by applying a voltage [48]. Surface alignment is the most established method so far for PVGs fabrication, as Figs. 2-9(a) and 2-9(b) depict. The second approach is to record the volumetric polarization field by applying the photocycloaddition of cinnamate groups or similar all-in-one materials. After the bulk LC alignment, the film is annealed to induce birefringence. This process is illustrated in Fig. 2-9(c).

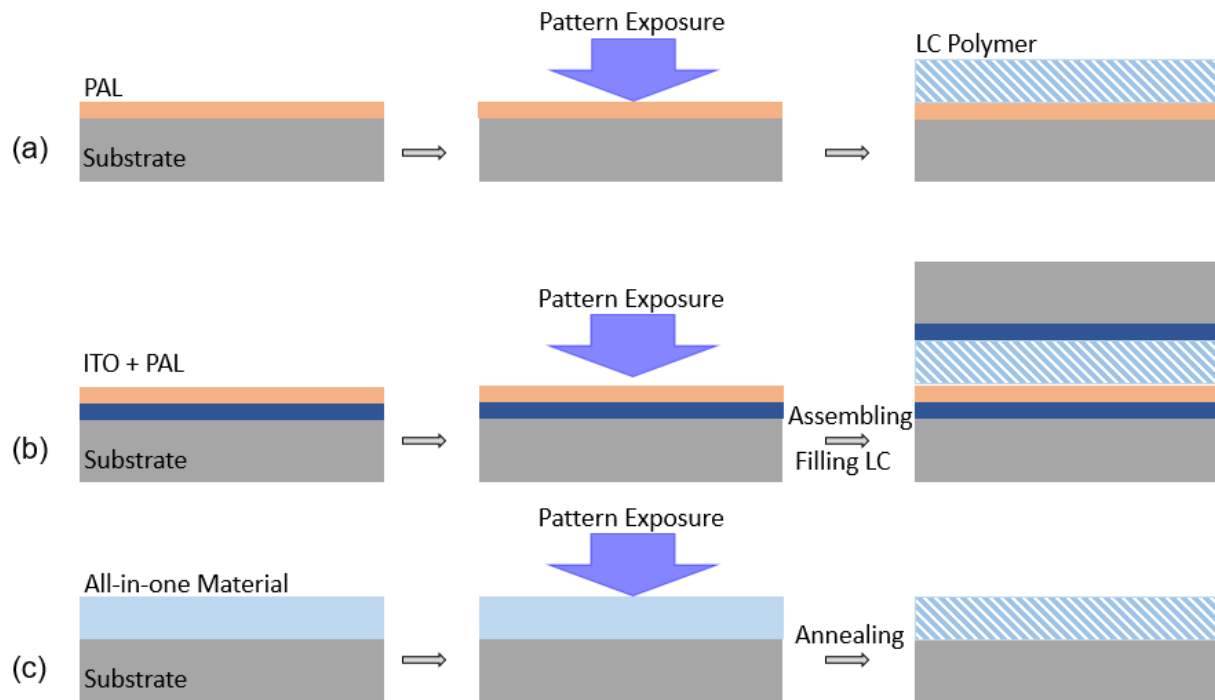


**Figure 2-9 Fabrication procedures of PVGs. (a) Surface alignment for LC polymeric PVG. (b) Electrically responsive LC PVG. (c) Volume alignment.**

The polarization field used to provide desired pattern on the PAL is usually generated by light exposure [49-51]. In the simplest case, the CLC reflector can be formed by a linearly

polarized light without any period, as shown in Fig. 2-10(a). Then for the grating with one-dimensional pattern, we need a polarization interferometer (Fig. 2-10(b)) to generate linearly changed period by two interfered beams. The laser beam is filtered and expanded, then split into two arms by a beam splitter (BS). A quarter-wave plate (QWP) is placed in each arm to convert the incident light to RCP (Path 1) and LCP (Path 2). Then these two beams are reflected by the mirrors (M) to interfere at the sample (S). Normally, the PVG phase can be obtained without other optical components in box A. However, appropriate modifications can be made to achieve exotic PVG phase profiles. For example, if a cylindrical lens is added, then the polarization field has an additional parabolic phase in one dimension, so that the fabricated PVG shows a period of gradient change according to the direction of the cylindrical lens. In addition, if a lens is added, then the final PVG would have an additional parabolic phase profile in two dimensions, which makes it no longer a grating, but a PVL.

Besides, the polarized light field for fabricating PVGs can also come from a pixelated spatial light modulator (SLM) [52-54]. As depicted in Fig. 2-10(c), the collimated linearly polarized laser beam is converted to circular polarization by a QWP, and then is reflected by a high-resolution SLM. The spatially modulated laser beam is changed back to linear polarization by the second QWP and imaged onto the substrate coated with the photo alignment material. The resolution of this method is limited by the pixel density of the SLM. If the period is too small to record, then a lens-system needs to be added to compress the pattern to meet the requirements. Although this method has some limitations, it still provides a possible solution for fabricating PVGs and other PVG-based devices with designed patterns.

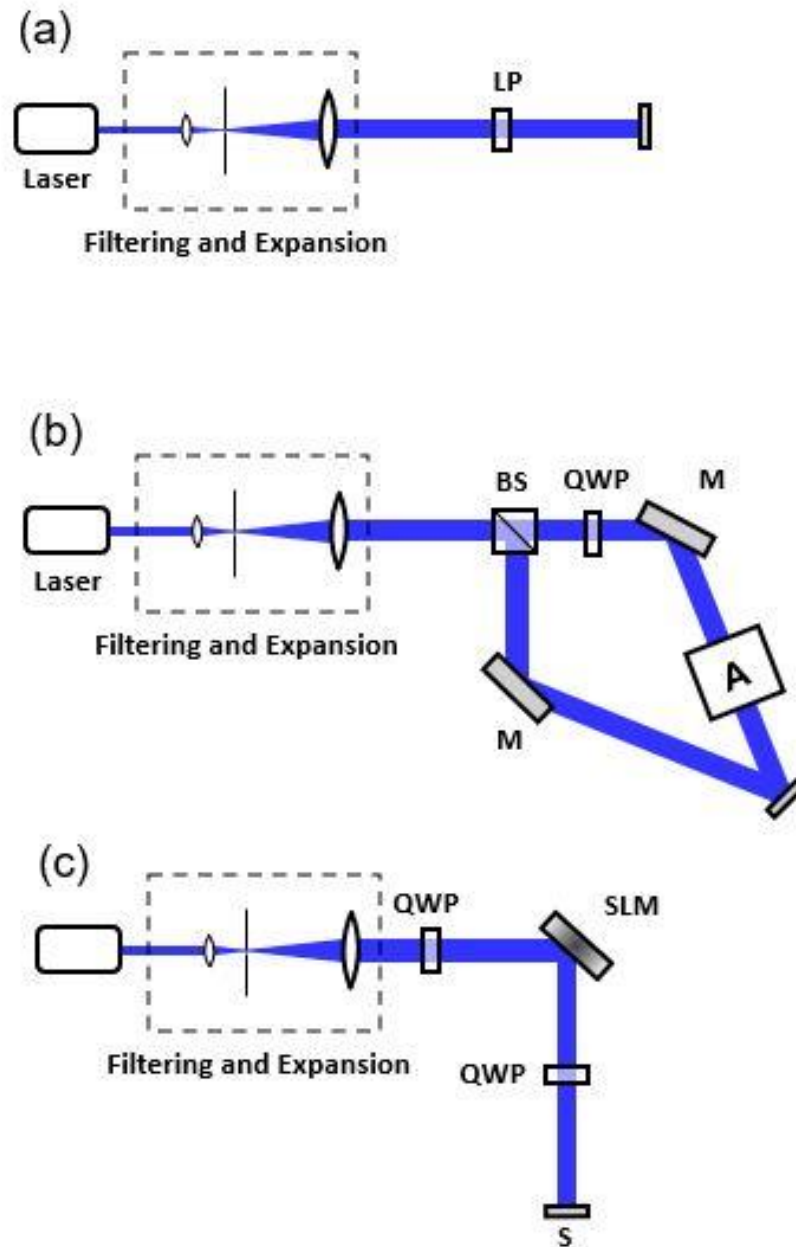


**Figure 2-10 Exposure setups of CLC devices. (a) CLC reflector exposure. (b) Two-beams interferometer for PVG and PVL. (b) Exposure based on phase pattern generated by SLM.**

## 2.4 Summary

In this chapter, we briefly summarize the optical properties and LC configurations of patterned CLC devices. The zero-dimension reflector shows mirror-like performance with angular and wavelength selectivity. The one-dimensional PVG is a kind of volume Bragg grating with high first-order efficiency and strong polarization selectivity. To characterize the diffraction behavior, we use the FEM model to simulate the response of different incident wavelengths and angles. The two-dimensional PVL can be treated as a combination of PVGs, therefore, having the same wavelength and angular responses.

Furthermore, the fabrication of patterned CLC devices is also summarized. Inside the device bulk, LC molecules follow the recorded pattern and precisely organize the vertical structures for building optical elements. Due to the high efficiency and polarization selectivity, patterned CLC devices with ultrathin form factors have found widespread applications in novel optical systems, particularly NEDs. We will discuss these applications in the following chapters.

## **CHAPTER 3 : FOVEATED IMAGING VR ENABLED BY CLC REFLECTOR**

### 3.1 Background

In this chapter, we will focus on the application of zero-dimension CLC reflector to solve the issues in VR displays. At present, the visual experience provided by commercial VR headsets is still significantly lower than that of human perception [11,55,56]. One of the reasons is inadequate angular resolution. The acuity of a normal person is around 1 arcmin, which is 60 pixels per degree (ppd), while most commercial VR displays can only offer 10 to 20 ppd, depending on the field of view [57,58]. Thus, the VR headset users can easily observe the screen-door effect, which significantly degrades the image fidelity.

A straightforward approach to match human-eye acuity is to increase the resolution density of the display panel. To achieve angular resolution  $\sim 60$  ppd and field of view  $>100^\circ$  simultaneously, each eye needs a display panel with at least 6K $\times$ 6K pixels [58]. With panel makers' vigorous efforts, commercial VR display resolution has reached 4K per eye. Recently, Pimax announced to release VR headsets with 6K resolution per eye soon, although there is still a long way to go for low-cost mass production. It's worth mentioning that the observed ppd is also affected by panel utilization and optical elements, meaning that even 6K resolution may still be insufficient. In addition, it would be extremely challenging to render high-resolution images and videos in real-time, and a more efficient image rendering pipeline must also be developed to support tremendous data transfer.

Therefore, foveated imaging becomes a more favorable solution to provide ultra-high-resolution images by considering the panel fabrication and data transport difficulties [58-62]. Due to the 1-arcmin requirement being only for the narrow central region ( $< \pm 5^\circ$ ) defined by the cone cell distribution on

retina, we may only need to provide high resolution for central fovea region instead of the entire FoV [63]. To achieve foveated VR display, current approaches employ two separate display panels to provide low-resolution and high-resolution images, respectively [58]. Aside from the two-panel requirement, a beam splitter cube/plate is required to combine the images of two panels, which will lead to a bulky system and high-power consumption.

Here, we propose and demonstrate a foveated VR system implemented by our polarization dependent mirror-like CLC reflector. Due to the strong polarization selectivity of CLC reflector, the low-resolution image and the high-resolution image are encoded into two orthogonal polarization states respectively, which are overlapped and displayed on the same display, and then be separated by the CLC reflector. One of the polarization images provides a wide FoV, just like a conventional VR display panel. The other provides an ultra-high resolution for the fovea through a polarization-dependent optical minification system, which increases the effective resolution. The proposed system can effectively suppress the screen-door effect while reducing the system volume and power consumption of the VR headset.

### 3.2 System Design

Figure 3-1 depicts the system configuration of the proposed foveated display design enabled by polarization-multiplexing. Briefly, this design consists of one display module, a half mirror, some optical lenses, and a polarization-dependent CLC reflector. The peripheral image and the center image are displayed on the same panel, and then be decoded into LCP and RCP light, respectively.

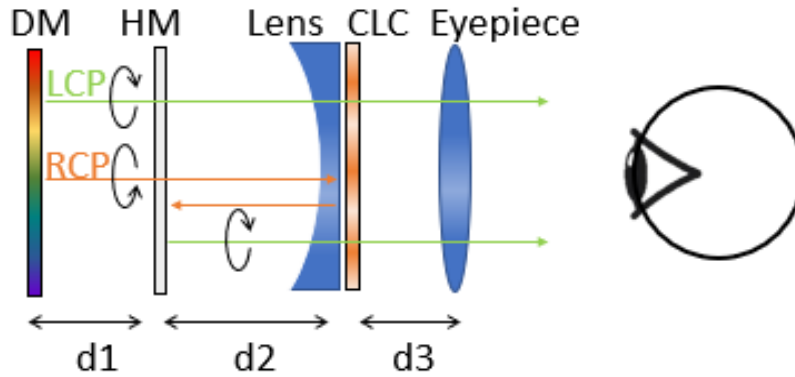


**Figure 3-1 Schematic diagram of the proposed multi-resolution foveated display for a VR headset. DM: Display module; HM: Half mirror; CLC: Cholesteric liquid crystal.**

The unfolded optical layouts of the proposed design are illustrated in Fig. 3-2(a) and 3-2(b). For one polarization state, say LCP, it passes through the system and enters the human eye, just like the conventional VR system. However, in our design this polarization only delivers the image content for surrounding region or peripheral image.

For the opposite polarization state, say RCP, the light will pass through a folded optical path. As illustrated in Fig. 3-2(b), the RCP light displays the center image, and the light will enter the concave lens three times. The first time is the same as LCP light, then it is reflected by the CLC reflector and arrives at the concave lens for the second time. After being reflected by the half mirror, the RCP will be converted to LCP, and the light will enter the concave lens for the third time. Finally, it passes through the CLC reflector and enters the human eye. Compared to LCP, the RCP light goes through the concave lens two more times, so the image will be minified thereby enhancing the resolution density.



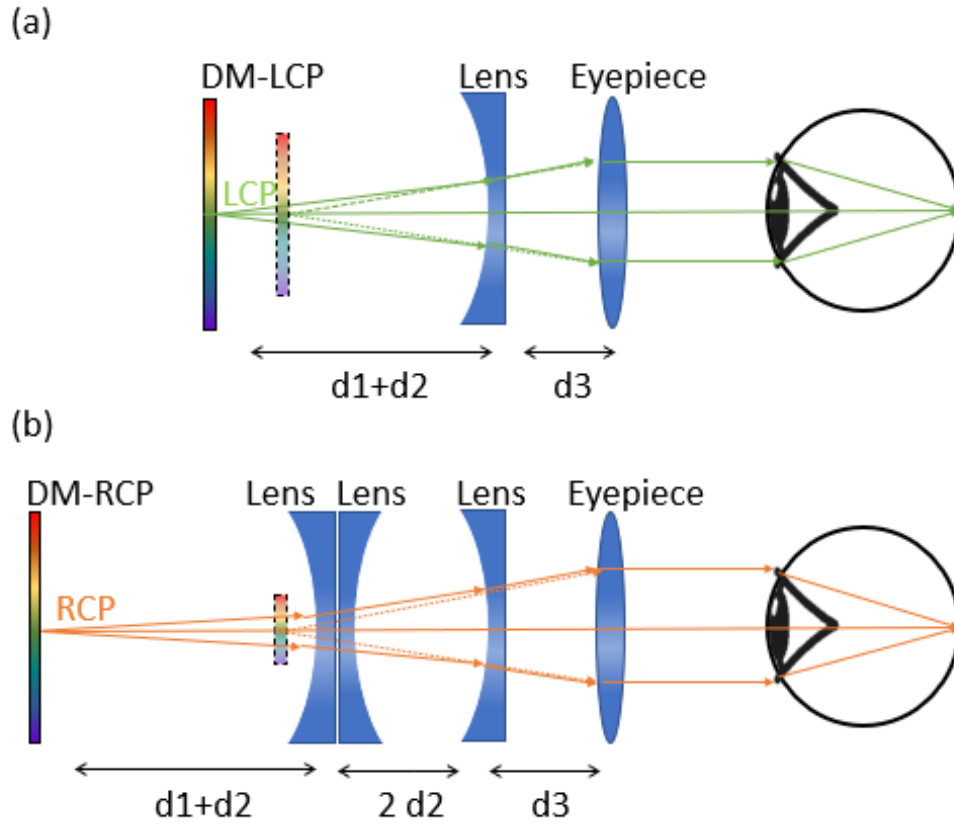


**Figure 3-2 The unfolded layout of the optical paths for (a) peripheral image with low resolution, and (b) center image with high resolution.**

If the focal length of the concave lens is denoted as  $-f$  and the optical minification factor between peripheral and center images as  $M$ , then the spatial resolution enhancement ratio  $R$  can be expressed as:

$$R = 1/M = 1 + 2(d_1 + d_2/f) \quad (3-1)$$

where  $d_1$  is the distance between the display module and the half mirror, and  $d_2$  is the distance from half mirror to CLC. According to Eq. (3-1), the enhancement ratio  $R$  can be enlarged by reducing the focal length  $f$  of the concave lens or increasing the distance  $(d_1+d_2)$ . In our following experimental demonstrations, the resolution enhancement can reach 4.4 times.

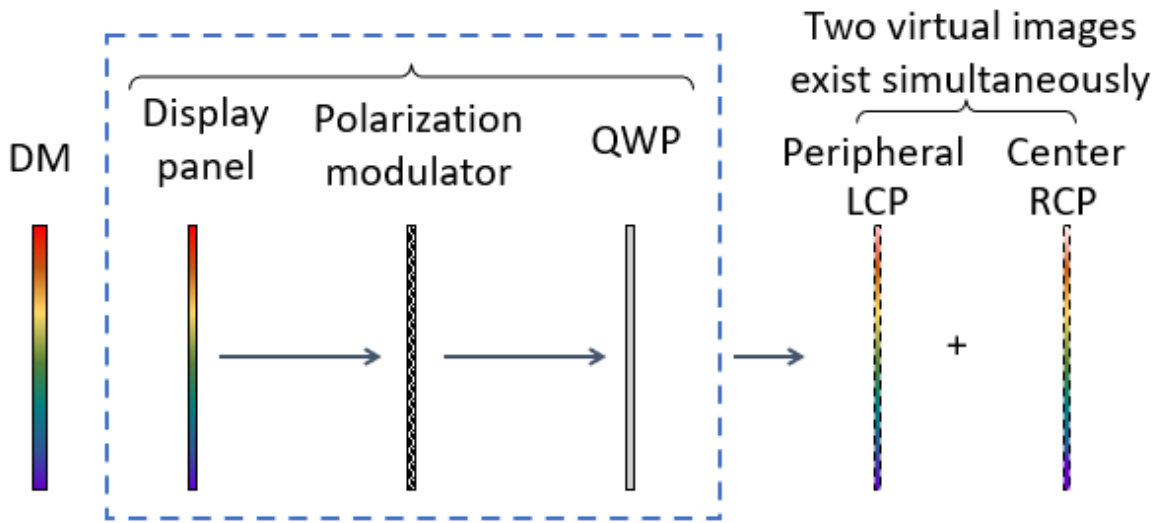


**Figure 3-3 Schematic diagram of the proposed polarization multiplexed display module, including a display panel (DM), a polarization modulator, and a broadband quarter-wave plate (QWP).**

In our proposed system, it is critical to display two images (peripheral and center images) on the same display panel while splitting them during the imaging process. Figure 3-3 depicts the configuration of our proposed polarization-multiplexed display module. The display module consists of three components: one display panel, one polarization modulator, and a broadband quarter-wave plate (QWP). The display panel can be a liquid crystal display which usually consists of two linear polarizers. Without losing generality, we can assume the display panel emits a linearly polarized light along the  $z$ -axis ( $0^\circ$ ). Then a pixelated polarization modulator is closely integrated and aligned to the display panel. The polarization modulator is designed to obtain full range between two orthogonal polarization states from  $0^\circ$  to  $90^\circ$  with continuous modulation including intermediate states. With a broadband  $\lambda/4$  plate oriented at  $45^\circ$ , these two orthogonal linear polarizations would be converted to LCP and RCP beams to present peripheral and center images, respectively. With the help of a CLC reflector, the LCP and RCP lights will be sent to two different optical paths simultaneously [64].

### 3.3 System Integration

To prove concept, we carried out a simple experiment to demonstrate our proposed design discussed above. Our optical setup follows the layout depicted in Fig. 3-1. In experiment, we used a 6.1-inch LCD (iPhone 11, with resolution  $1792 \times 828$ ) as the display panel. To prepare a polarization modulator, we removed the polarizers of a commercial twisted nematic (TN) LCD panel (5.0 inch,  $800 \times 480$  pixels) and used it as polarization modulator. One plano-concave lens with focal length  $f = -35$  mm was adopted.

To obtain a full color polarization-selective reflector, we stack three CLC reflectors together. Such a CLC reflector exhibits a helical structure; it reflects the circularly polarized light with the same handedness, (e.g., RCP), but transmits the opposite polarization (LCP). The central wavelength ( $\lambda_0$ ) of the Bragg reflection is jointly determined by the CLC reflector helical pitch length ( $p$ ) and average refractive index ( $n$ ) of the employed LC material as  $\lambda_0 = pn$  [65]. Each CLC reflector has the central wavelength located at red, green, and blue, respectively. The blue and green CLC reflectors were spin-coated on two separate 2-inch glass substrates, and the red one was spin-coated on top of the blue one, as Fig. 3-4 shows.

In experiment, we used RM257 (from LC Matter) as LC monomer, whose average refractive index is 1.508 and birefringence is 0.152, 0.161, 0.176 at 630 nm, 530 nm, 450 nm, respectively. S5011 (from HCCH) was chiral dopant, which made the LC directors rotating along the helical axis. By adjusting the concentration of chiral dopant, the CLC pitch length can be changed, and the central wavelength of Bragg reflection can be tailored to a desired value. The CLC film has three layers, and each layer has the central wavelength located at red, green, and blue spectrum, respectively. In our design, the helical pitch length for the RGB layers is around 417

nm, 351 nm and 298 nm, respectively, and the thickness of each layer ( $\sim 3\text{-}4\ \mu\text{m}$ ) is restricted to  $\sim 10$  helical pitches by controlling the ratio of solute and solvent in the CLC solution, and the speed of spin-coating. The blue and green CLC layers were spin-coated on two separate 2-inch glass substrates, and the red one was spin-coated on top of the blue one. Then the two substrates were laminated together to form a three-layer CLC polymer film, which was robust and thermoresistant. If we fabricated two layers with close central wavelength together (e.g. blue and green, or green and red), then the two reflection bands will merge into one, because RM257 has a relatively high birefringence and the reflection band is broad.

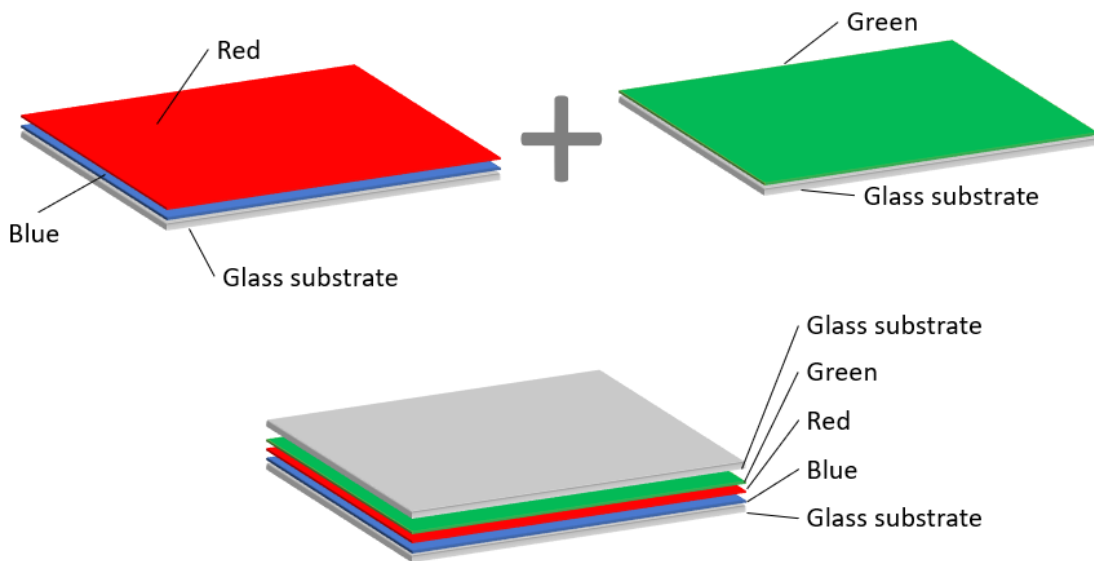


**Figure 3-4 Schematic illustration of the three-layer cholesteric LC reflector.**

Next step is to generate the image displayed on the panel. Since we only use one panel, the images of peripheral and center fovea areas need to be overlapped and displayed on the same panel, but with different sizes. The peripheral image is shown in [Fig. 3-5\(a\)](#). The center image comes from the content that should be displayed in the blank area of the peripheral image. Because we

will minimize the center image to increase the resolution in the following optical system, the center image here is enlarged by 4.4x, as shown in [Fig. 3-5\(b\)](#). After passing through the following optical system, the size of the center image will fit the blank in peripheral image and become a complete whole image again. Then we combine these two images together with designed ratio and generate the image that we need to display on the panel. [Figure 3-5\(c\)](#) is the computer-generated image for the display panel, in which the peripheral and the central areas overlap each other but can be clearly distinguished.

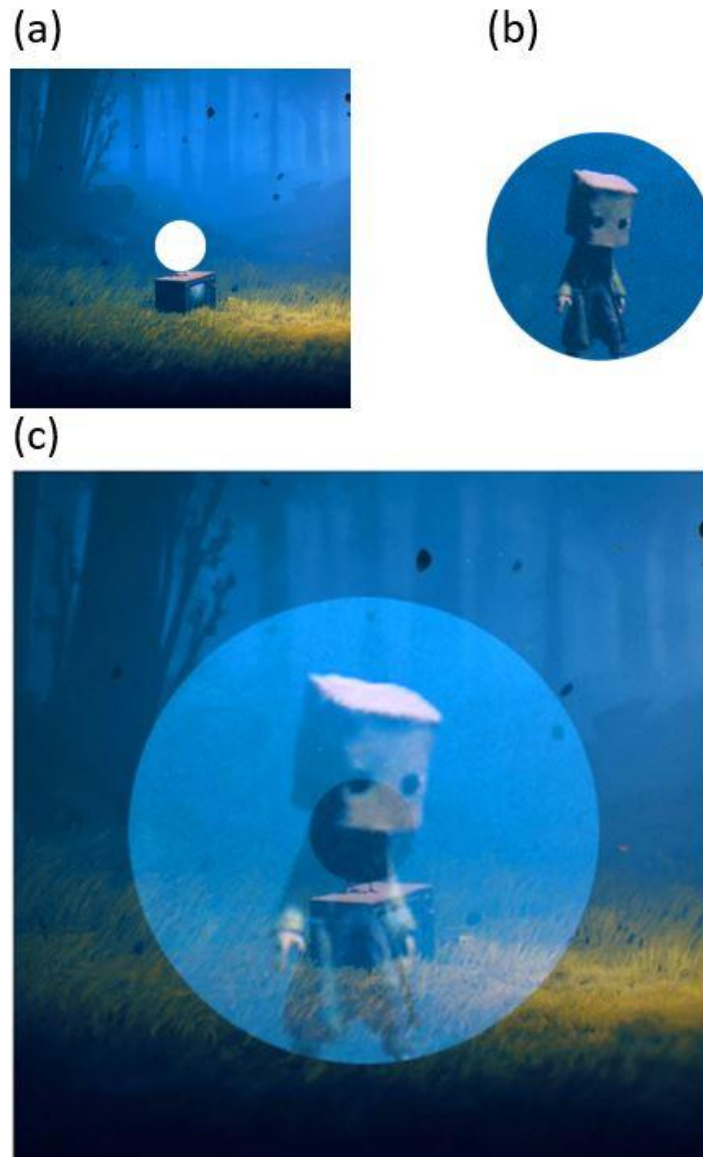


**Figure 3-5 The displayed image: (a) peripheral image, (b) enlarged center image, and (c) combined image on the display panel.**

Then, we build the setup and all the optical elements we used are listed in [Fig. 3-6](#). [Figure 3-7](#) represents the experimental results. The center image area is minimized by the polarization-dependent optical system to fit the blank area with higher resolution. This complete image with multi-resolution is shown in [Fig. 3-7\(a\)](#). In [Figs. 3-7\(a\)](#) and [3-7\(b\)](#), the displayed image region,

enclosed by yellow dashed lines, exhibits a much higher angular resolution than that of the outside regions. When we zoom in the center area enclosed by the green rectangle, the apparent pixelation and screen-door effect can be observed in the outside low-resolution region in Fig. 3-7(b). While inside the yellow dashed circle, the image is quite smooth. By further zooming in the photographs, the pixel size can be compared directly at the boundary, as depicted in Figs. 3-7(c) and 3-7(d).

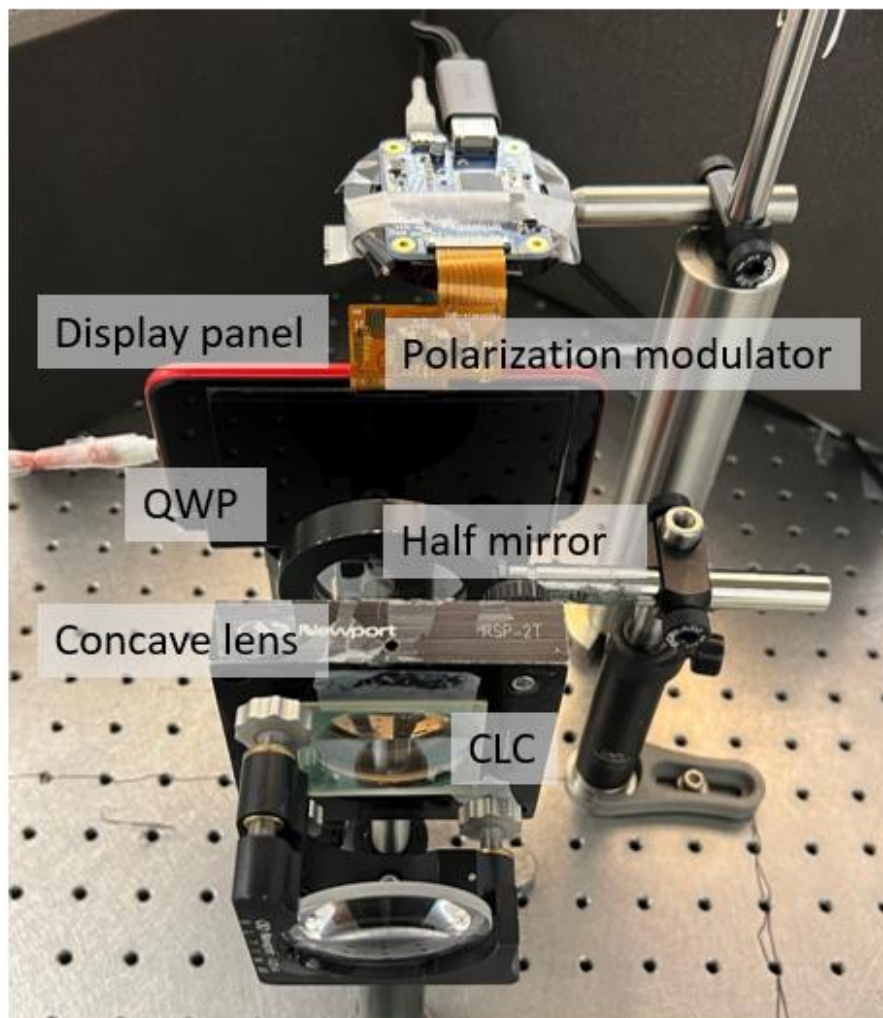


**Figure 3-6** Picture of the benchtop demo and optical elements used in the system.

For quantitative evaluations, we can easily measure the center image size before and after the minification system. Since the peripheral and center images are displayed on the same panel at the beginning, they possess the same resolution. Then, the center image passes through the polarization-dependent optical paths to accumulate different optical power. By comparing the center image size in Fig. 3-5(c) and Fig. 3-7(a), the diameter of the image is reduced by 4.4x, which is corresponding to the resolution enhancement ratio. Besides, the resolution enhancement ratio of the central region can be easily tuned by changing the focal length of the concave lens or the distance ( $d_1+d_2$ ) as Fig. 3-2 depicts. A higher resolution is achievable, but the trade-off is increased system volume and more challenging lens design.

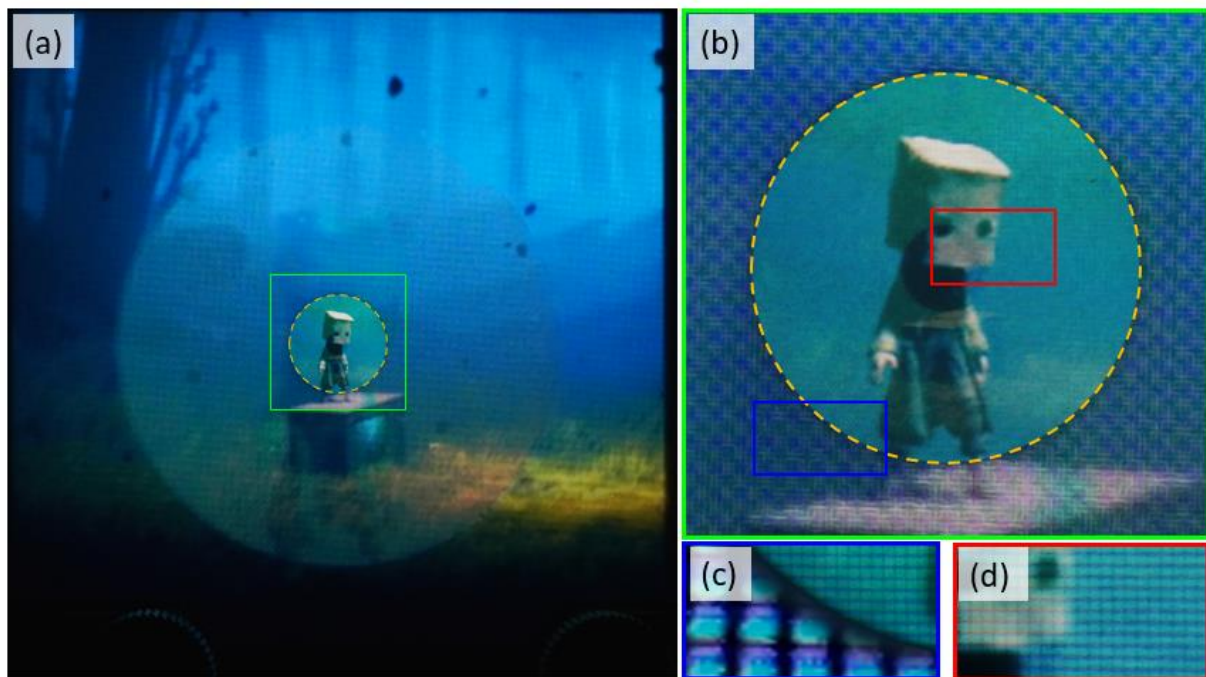


**Figure 3-7 Experimental photographs of the proposed multi-resolution display with 4.4x resolution enhancement: (a) whole displayed image; (b) the magnified green square region in (a); (c) the magnified blue rectangle region in (b); (d) the magnified red rectangle region in (b).**



### 3.4 Summary

In this chapter, we experimentally demonstrated a multi-resolution foveated display for VR applications. The novel system is achieved by RGB CLC reflectors with strong polarization selectivity. Compared to conventional foveated imaging systems, the proposed design only requires one display panel without the need for a beam splitter. By using the polarization multiplexing method, we encode the peripheral images and the center images into two orthogonal polarization states, and then send them to two optical paths with different optical powers. As a result, an ultra-high resolution for the central fovea region can be obtained. The spatial resolution of the fovea area is enhanced by 4.4x by an optical minifying system. The proposed optical system can effectively reduce the screen-door effect while providing a compact system design for near-eye displays.

## CHAPTER 4 : WAVEGUIDE AR ENABLED BY PVG

### 4.1 Background

In the past few decades, AR displays, such as Google Glass, Microsoft HoloLens, and Magic Leap One, have found interesting applications in areas such as education, healthcare, engineering, and gaming [66,67]. To integrate the computer-generated (CG) images with see-through real-world environment, different types of optical combiners have been developed. For examples, the polarizing beam splitter (PBS) is used in traditional optical design, and the partial mirror and grating are widely used in waveguide design. Compared to the PBS approach, waveguide-based AR offers several attractive features, such as compact structure and lightweight.

In this waveguide type AR device, the display light is collimated and deflected into thin waveguides through an input-coupler. After traveling to the viewing region through total-internal reflection (TIR), the light is again deflected toward the observer's eye by an output-coupler. The input- and output-couplers are large-angle deflectors that are currently made with holographic volume gratings (HVGs) and surface-relief gratings (SRGs). Common holographic volume gratings are isotropic materials with alternative slanted layers of high and low refractive indices. The angular bandwidth for a single holographic volume grating is determined by the index contrast. Holographic volume gratings based on dichromated gelatin can provide an index contrast as high as 0.15; however, dichromated gelatin-based holographic volume gratings are sensitive to environmental conditions such as humidity and temperature and are therefore unstable for commercial applications. Nowadays, most of the design adopted photopolymers as recording media with index contrast around 0.035 [68]. As a result, the deflection has a high angle/wavelength selectivity. This allows almost 100% transmittance of the environment light; however, this also translates into a very low efficiency for the display light, causing a

high-power consumption. To widen the FoV while maintaining flat profile, multiple layers of holographic volume gratings are exploited. This not only reduces the transmittance but also greatly increases the device cost.

The polarization-sensitive counterpart of holographic gratings, often referred to as holographic polymer-dispersed liquid crystal (HPDLC) [69,70], exploit electrically responsive birefringent liquid crystal materials and therefore can allow switchable grating couplers with higher index contrast. Fabrication challenges exist for high quality holographic gratings and HPDLCs due to the inhomogeneity induced during the diffusion process, resulting in optical imperfections in the structure [70]. Surface-relieve gratings, on the other hand, exploit alternate air-polymer slanted structure, and therefore can theoretically achieve a higher index contrast with better efficiency and large angular acceptance. However, it is challenging to achieve ideal optical efficiency in mass production due to the difficulty in replicating oblique high-aspect-ratio grooves [71].

Therefore, the PVGs with nearly 100% efficiency and large diffraction angle become the perfect candidate for the waveguide AR system as the input and output couplers. Figure 4-1 shows the basic structure of waveguide AR by using PVG as the couplers.

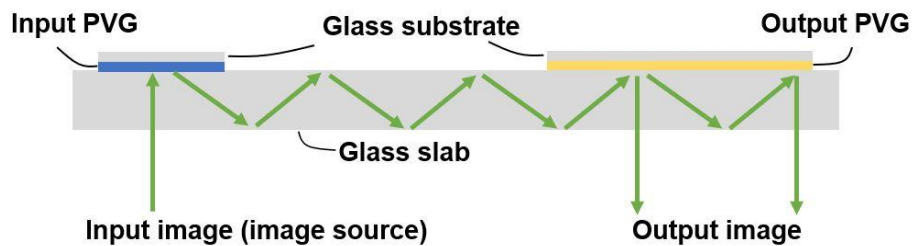


**Figure 4-1 Illustration of waveguide AR with PVGs as input and output couplers.**

Compared to HVGs and SRGs, PVGs exhibit unique characteristics in both optical properties and fabrication, such as high index contrast ( $\sim 0.18$ ), strong polarization selectivity, and a simple fabrication process. The pioneering work on reflective PVGs has experimentally achieved 95% diffraction efficiency. In addition, a stretchable and flexible PVG film is also investigated [29]. However, the angular bandwidth is still inadequate for AR waveguide applications [72].

In this chapter, we focus on the chirped polarization volume grating (CPVG) with ultra-wide angular bandwidth for expanding the FoV of see-through NEDs. The CPVGs, with the grating period gradually changing along the beam propagation, not only inherits the advantages of PVGs but also triple the angular bandwidth. We fabricated such a wide-angular-bandwidth CPVG and characterized its performance. The measured results are consistent with the simulation ones using the finite-element method (FEM). Besides, we also investigate the performance of multi-layer PVGs by simulation. In experiment, we fabricated a two-layer PVG and compared its performance with CPVGs. Then we apply this CPVG into waveguide AR as the coupler to enlarge the FoV.

## 4.2 Achieving CPVGs

For PVG, the horizontal periodicity ( $P_x$ ) is defined as the distance by which LC directors rotate  $180^\circ$  along the horizontal direction, and the vertical periodicity ( $P_y$ ) is the distance by which LC directors rotate  $180^\circ$  along the vertical direction. In order to obtain a wider angular bandwidth, we induce gradually changing period along  $y$  direction as a modulation while the period along  $x$  direction is fixed, as shown in [Fig. 4-2](#).

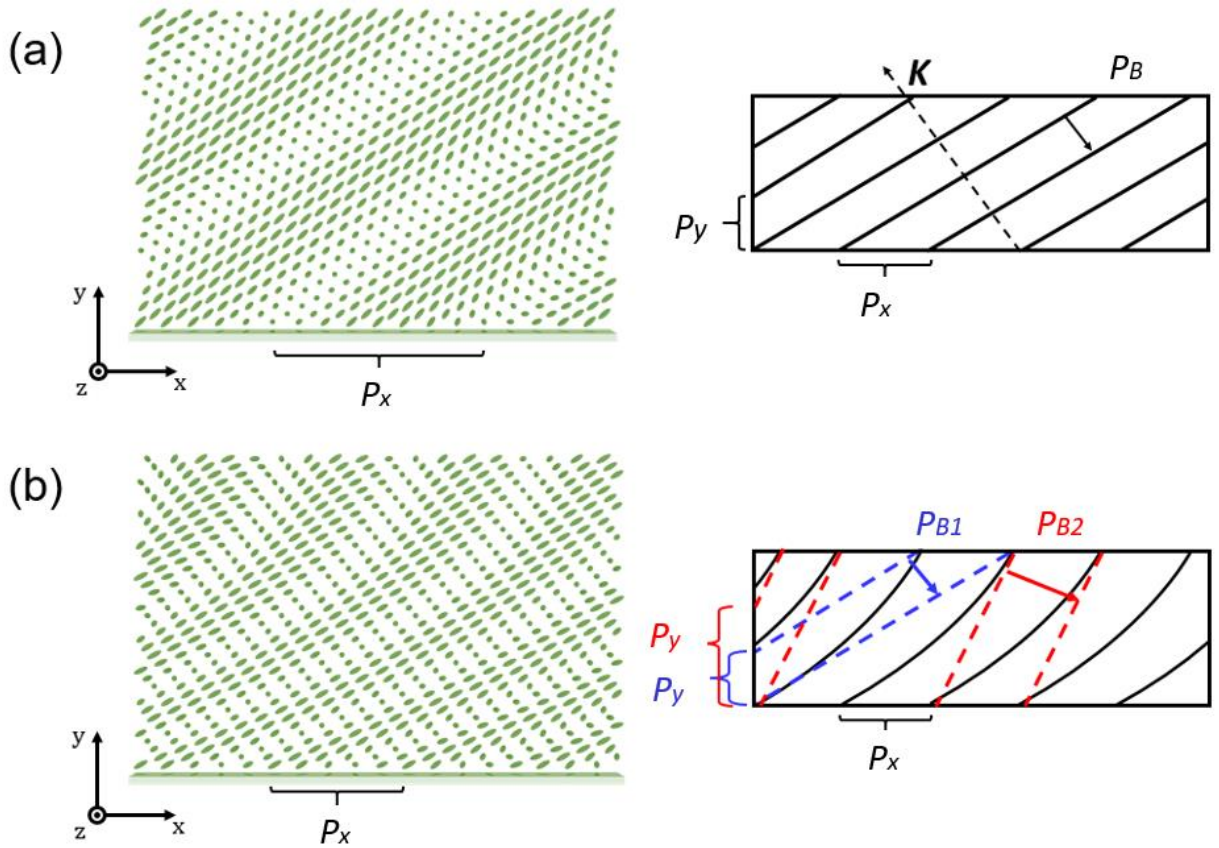


**Figure 4-2 LC director profile of the uniform PVG and CPVG. (a) The horizontal period is  $P_x$ , the vertical period is  $P_y$ , and the Bragg period is  $P_B$ . (b) The horizontal periodicity is  $P_x$ , the vertical periodicities are  $P_{y1}$  and  $P_{y2}$  at the bottom and top, respectively, and the Bragg period are  $P_{B1}$  and  $P_{B2}$  at the bottom and top, respectively.**

Several approaches to generate gradient pitch in CLC have been reported in [73,74]. By adding UV dye into the PVG precursor, raising the curing temperature, and decreasing the power of UV curing light, we can precisely control the length of  $P_B$ , which is determined by the CLC structure. As reported in [75], the  $P_B$  along the helical axis is defined by:

$$\frac{1}{P_B} = \frac{1}{P_{B1}} + \left(\frac{1}{P_{B2}} - \frac{1}{P_{B1}}\right) \frac{s}{t}, \quad (3-1)$$

where  $t$  is the total length of the helical axis and  $s$  is the coordinate along it, and the period length is gradually changing from  $P_{B1}$  ( $s=0$ ) to  $P_{B2}$  ( $s=t$ ). Keeping  $P_x$  as a constant, we derive the variation of  $P_y$  along  $y$  direction in CPVG as:

$$1/P_y = 1/P_{y1} + (1/P_{y2} - 1/P_{y1})y/d + o((P_{y1} - P_{y2})^2 / P_{y1}^3), \quad (3-2)$$

where  $P_{y1}$  and  $P_{y2}$  are the period lengths along  $y$  axis near the bottom surface and top surface, respectively, and  $o$  means the higher-order terms. Generally,  $(P_{y1} - P_{y2})^2 / P_{y1}^3$  is much smaller than 1 so that this term can be omitted safely, similar to that reported in [30]. Furthermore, the equation of the isophase line in CPVG can be expressed as:

$$\varphi = \pi/P_x x + \pi/P_y y + (\pi/P_{y2} - \pi/P_{y1})y^2/d, \quad (3-3)$$

where  $P_x$  is the period length along  $x$  axis and  $d$  is the thickness of CPVG. Once the isophase line equation is derived, we can obtain the LC orientations inside the CPVG. These orientations define the dielectric constant matrix, which is the key parameter in the simulation. Compared to a uniform PVG, the gradient pitch profile generates a series of refractive index planes with gradually changing slope.

In simulation, we assume the birefringence of RM257 is  $\Delta n = 0.18$  ( $n_e = 1.68$ ,  $n_o = 1.50$ ) at  $\lambda = 532$  nm and the thickness of the grating is 5  $\mu\text{m}$ . For a uniform PVG, the period length along  $x$  and  $y$  directions are set as  $P_x = 462$  nm and  $P_y = 203$  nm. In terms of CPVGs, the length of  $P_{y1}$  and  $P_{y2}$  are set as 192 nm and 203 nm, respectively. The simulated angular response for the gradient pitch (CPVGs) and uniform pitch (PVGs) are depicted in Fig. 4-3. The black curve in Fig. 4-3 shows the angular bandwidth of such a uniform PVG is around  $17^\circ$  ( $-8^\circ$  to  $9^\circ$ ) at 90% efficiency (marked with red dashed lines). In comparison with uniform PVGs, CPVGs have the angular

bandwidth of  $55^\circ$  (from  $-8^\circ$  to  $47^\circ$ ) with diffraction efficiency over 90%. Our results clearly demonstrate that inducing gradient pitch significantly broadens the angular bandwidth.

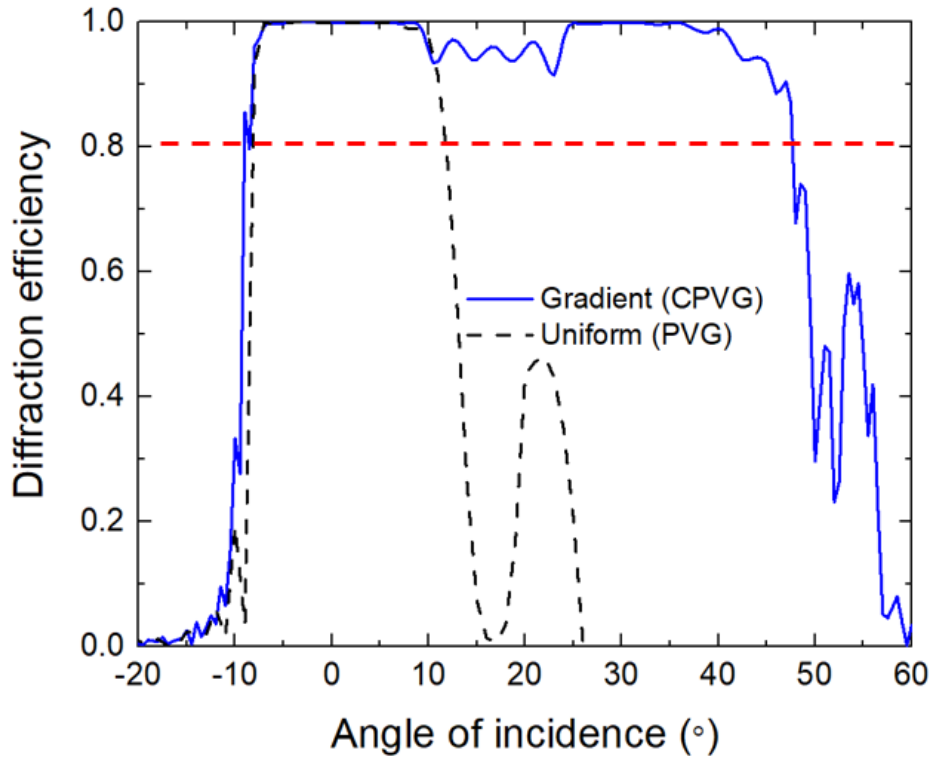


**Figure 4-3 Simulated first-order diffraction efficiency. Angular response at  $\lambda = 532$  nm of both gradient pitch CPVGs (blue line) and uniform pitch PVG (black line).**

We also simulate the angular and spectral bandwidth of CPVGs, and results are shown in [Fig. 4-4\(a\)](#). Besides, we also simulate the angular response in other directions. [Figure 4-4\(b\)](#) shows all the angular response in the two-dimensional plane. In  $x$ -direction, the angular response is asymmetric, by contrast, it is uniform and symmetric in the  $y$ -direction.

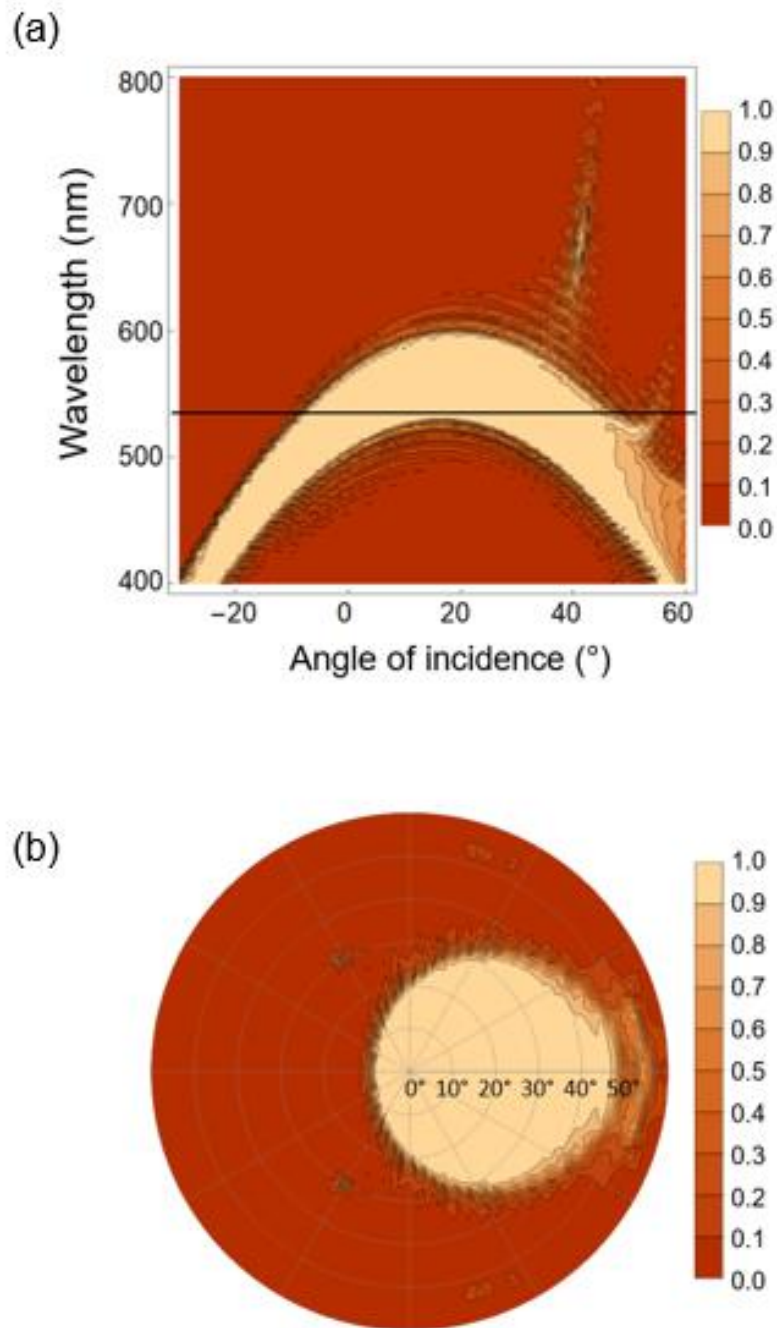


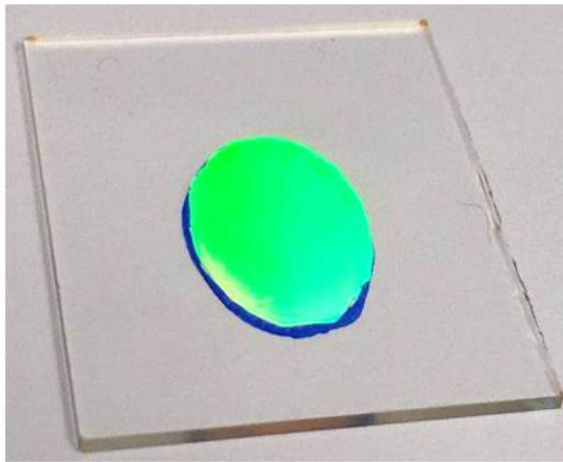
**Figure 4-4 (a) Simulated angular and spectral responses of the CPVGs. The black line shows the  $\lambda=532$  nm. (b) The two-dimensional angular response of gradient-pitch PVG.**



### 4.3 CPVG Fabrication

The fabrication procedure of reflective CPVGs is described in [76]. We firstly spin-coated brilliant yellow (BY, dissolved in dimethylformamide with 0.40 wt%) onto a cleaned glass substrate as photo-alignment layer, and then put the sample in a Mach-Zehnder interferometer ( $\lambda = 488 \text{ nm}$ ) to get exposure. The two-beams that interfere at the sample are LCP and RCP, respectively. Next, we spin-coated the PVG precursor onto the exposed sample. The mixture consisting of 1.50 wt% UV dye (Avobenzone), 2.48 wt% chiral agent R5011 (HCCH, helical twisting power HTP  $\approx 108 \mu\text{m}^{-1}$ ), 3.00 wt% initiator Irgacure 651, and 93.02 wt% photocurable monomer RM257 (HCCH) was diluted in toluene. To generate gradient pitch, the sample was placed on a hot plate at  $60^\circ\text{C}$  and cured with UV light ( $\lambda = 365 \text{ nm}$ ) for 40 minutes in nitrogen environment. Then a CPVG working on green (532 nm) light was obtained. By controlling the concentration of the chiral agent, we can easily get different central wavelengths in the visible range, such as red (633 nm) and blue (473 nm).

As Fig. 4-5(a) shows, the photo is viewed at  $50^\circ$  to clearly see the diffracted green light from the CPVG sample, where the CPVG region is circled by the blue line. The text shown in Fig. 4-5(b) was imaged through the sample. The distance between CPVG and camera is 1 cm, and the target is 10 cm away. The clear image seen through the CPVG region (encircled by the blue line) indicates that the scattering of the grating film is negligible. Due to the handedness selectivity, this CPVG allows more than 50% transmittance of the ambient light when the circularly polarized input is outcoupled at 80% efficiency.



(a)

Using  $S_2 = \frac{1}{2c} [b + \sqrt{b^2 - 4ac(T_2 - T^*)}]$ , we can see  
 In reality, there are usually irregularities, such as the energy barrier against the isotropic–nematic transition before the thermodynamic instability limits (superheating). In an optical microscope, it is usually observed that the transition is initiated by irregularities and growing out there. These isotropic ‘lakes’ are produced by irregularities and are called nucleation seeds and the transition from the nematic–isotropic transition is a first-order transition. Thus, there is an energy barrier against the transition. Therefore, there is superheating and supercooling. In such a case, the transition occurs simultaneously everywhere (at a certain temperature).  
 There are a few points worth mentioning in 1

(b)

**Figure 4-5** The CPVG sample viewed from an oblique angle with the CPVG region circled by a blue line. (b) A photo taken through the CPVG sample, where the CPVG region is circled by a blue line. The distance between PVG and camera is 1 cm, and the target is 10 cm away.

Next, we measured the angular response of CPVG using a circularly polarized green ( $\lambda=532$  nm) laser diode, and results are shown in Fig. 4-6. The angular bandwidth is  $54^\circ$  (from  $-7^\circ$  to  $47^\circ$ ) at 80% diffraction efficiency. Compared to a uniform PVG, the angular bandwidth is 3x wider. By introducing chirped structure to conventional PVGs, we can obtain a wider angular bandwidth, while keeping high efficiency and low scattering for a large-FoV AR display. The angular bandwidth of CPVG is  $\sim 2x$  wider than that of SRGs, and  $\sim 3x$  wider than that of PVGs and HVGs. Besides, the experimental data agree with the simulation results reasonably well, although the measured diffraction efficiency is about 10% lower than the simulated one. The main reason is that the LC alignment is quite sophisticated, including horizontal subwavelength period and vertical gradient period. Any disturbed alignment would decrease the diffraction efficiency.

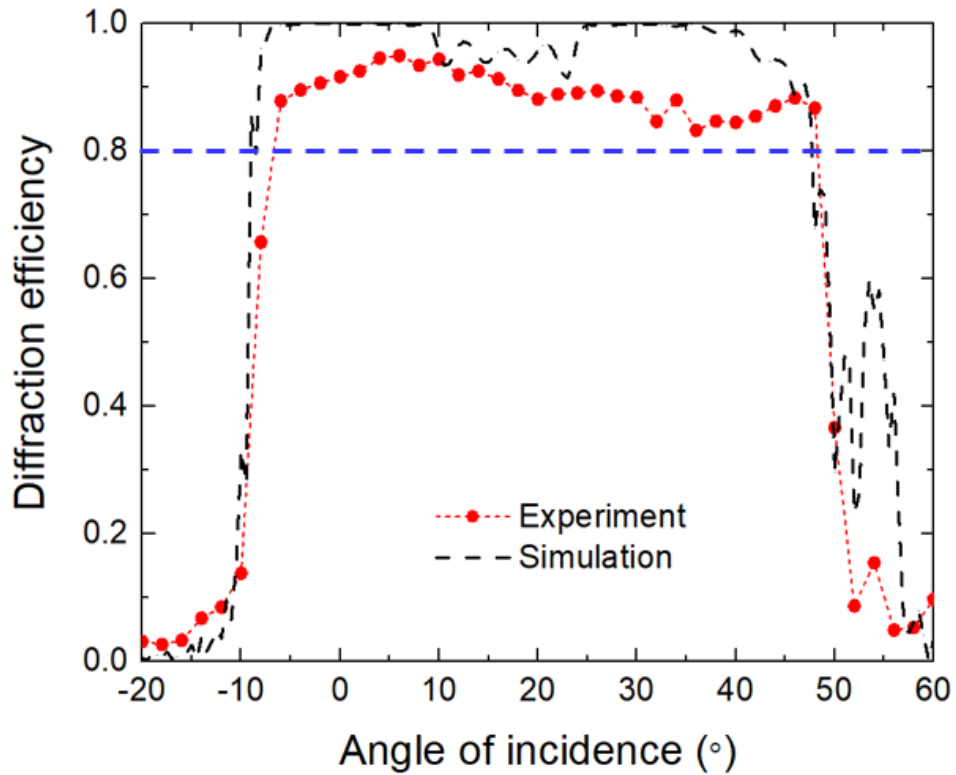


**Figure 4-6 Angular behavior of optical efficiency.** The black line is the simulation results, and the red dots denote the measured results of CPVG sample.

#### 4.4 Multilayer PVG

The CPVGs exhibit excellent optical properties and simple fabrication process. Similar to gradually changing period, discretely changed period can also extend the angular bandwidth. [Figure 4-7\(a\)](#) illustrates the concept of multi-layer structure. When the number of layers  $N$  approaches positive infinity, the multi-layer PVGs behave like CPVGs. Therefore, we would like to compare the performance of multi-layer PVGs with CPVGs. [Figure 4-7\(b\)](#) shows the example that  $N=2$ .

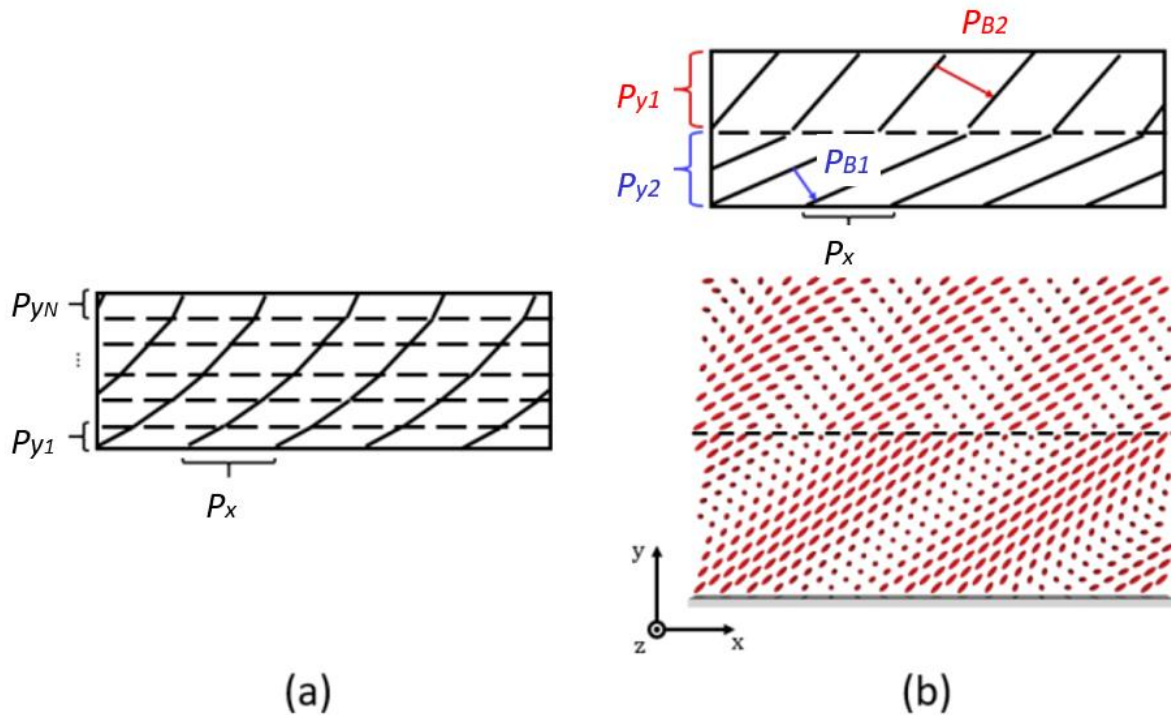


**Figure 4-7 (a) LC director profile of a multi-layer PVG. (b) Two-layer PVG.**

To fabricate a two-layer PVG, two different precursors are used. The first mixture consisting of 2.31 wt% chiral agent R5011, 3.00 wt% photo-initiator Irgacure 651, and 94.69 wt% photocurable monomer RM257 was diluted in toluene. The second mixture consisting of 2.62 wt% R5011, 3.00 wt% Irgacure 651, and 94.38 wt% RM257. To generate two-layer structure, the first mixture was spin-coated and then cured with UV light ( $\lambda = 365$  nm, 12 mW) for 5 minutes in nitrogen environment. Next, the second mixture was spin-coated onto the first layer and cured at the same conditions. The multi-layer PVGs can also be fabricated following this strategy. We measured the optical properties with a glass cylinder container filled with index matching oil ( $n = 1.58$ ). The CPVG sample was mounted on a rotatable stage and the whole unit was immersed in the container. The incident light was normal to the CPVG at the initial state, and the angle of incidence can be adjusted by rotating the CPVG. The first-order diffracted beam was measured by

a power meter. The efficiency is defined as the intensity of the diffracted beam to that of the reference beam passing through the glass cylinder with index matching oil and glass substrate only (without CPVGs).

Then we compare the simulation results and experimental results. In simulation, we assume  $\Delta n = 0.18$  at  $\lambda = 532$  nm. To keep consistency, the parameters of uniform PVGs are still set as  $P_x = 462$  nm and  $P_y = 203$  nm. For the two-layer PVG, the period length is assumed to be  $P_x = 462$  nm along  $x$ -axis, and  $P_{y1} = 190$  nm and  $P_{y2} = 220$  nm along  $y$ -axis and the thickness of each layer is  $2.5$   $\mu\text{m}$ . The simulated and measured angular responses for the two-layer PVG are depicted in [Fig. 4-8](#). The angular bandwidth of the two-layer PVG can also be extended to  $60^\circ$ , but the average efficiency is lower than 80%. The measured results generally agree with the simulated ones, except for lower optical efficiency. Due to the two-layer structure, the alignment of the second layer is highly dependent on the alignment of the first layer. Any defect in the first layer will affect the following layers, which in turn leads to decreased optical efficiency. The angular bandwidth of the two-layer PVGs is experimentally extended to  $65^\circ$  (from  $-10^\circ$  to  $55^\circ$ ) with 20% diffraction efficiency and average efficiency of more than 60%. It is worth noting that there are two deep valleys (at  $0^\circ$  and  $40^\circ$ ) in the angular response band. The diffraction efficiency at the valleys drops significantly, so this two-layer PVG is not suitable for AR displays that require a uniform image with high efficiency [77].

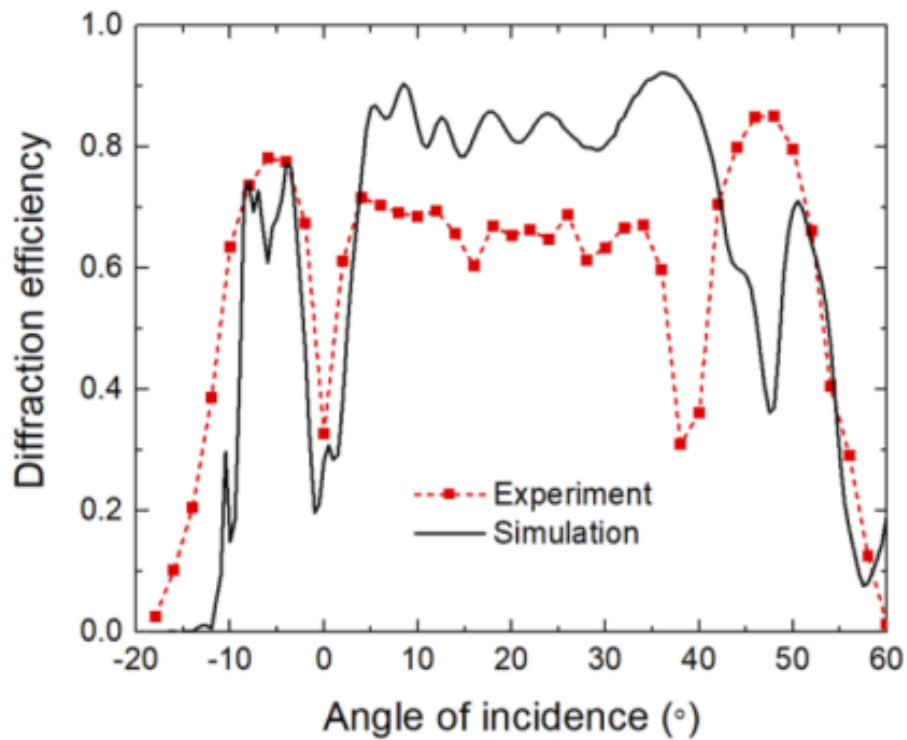


**Figure 4-8 Simulated and measured angular behavior of two-layer PVG.**

Here we only fabricate a two-layer ( $N = 2$ ) structure to illustrate the calculation methods and fabrication process of a multi-layer structure. As the number of layers increases, the multi-layer PVGs will behave like CPVGs. The simulation results ( $N = 1, 2, 3$ ) are shown in [Fig. 4-9](#).

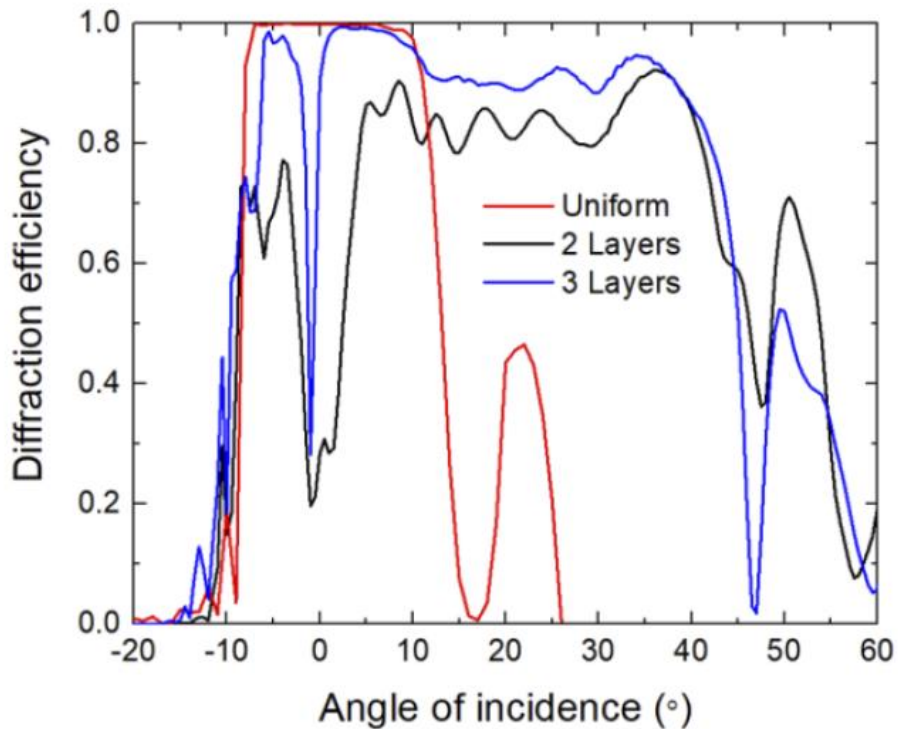


**Figure 4-9 Simulated first-order diffraction efficiency and angular response at  $\lambda = 532$  nm of uniform PVG (red line), two-layer PVG (black line), and three-layer PVG (blue line).**

In comparison with CPVGs, the biggest challenge for achieving wide angular bandwidth in multi-layer PVGs is not the optimization method but the fabrication process. Due to the roughness on the top surface of polymerized LC film, it is not easy to precisely control the thickness and the twist angle of each layer. The more layers we need, the more defects will be induced into the volume gratings. In addition, the LC molecules follow the pattern of the previous layer, therefore any kind of defect including unfollowed molecules or dust will have a serious effect on all the following layers.

#### 4.5 System Integration

For now, we have the CPVGs and multilayer PVGs. Then we will apply the CPVGs into the waveguide AR as the input and output couplers [78]. Figure 4-10(a) illustrates the structure of a simplified AR optical system with input/output couplers and image source. When the light enters the input CPVG, it would be diffracted into the waveguide with a designed angle, then propagates following the TIR. After hitting the output CPVG, the light would be diffracted out of the waveguide into the observer's eye.

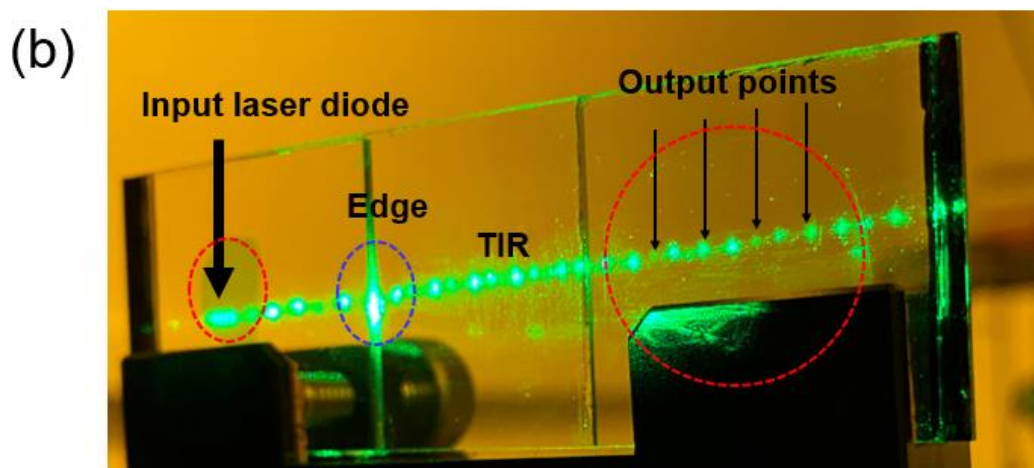
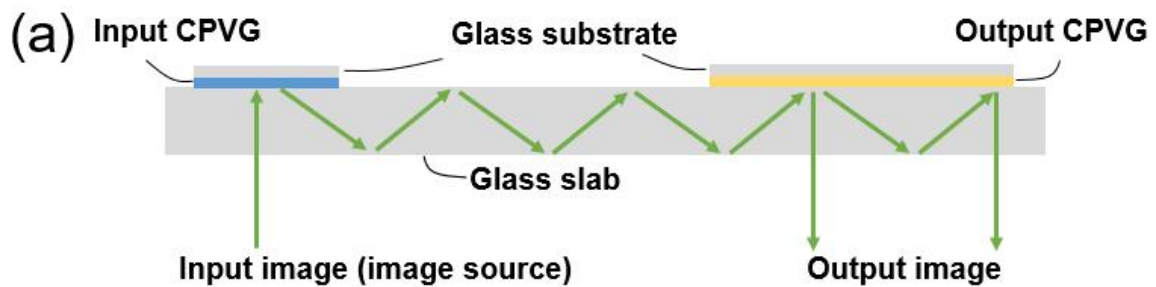


**Figure 4-10 (a) Top view of a simplified AR module. (b) Photo of an AR module with a green laser diode input light.**



To demonstrate the feasibility of CPVG for AR displays, we fabricated two CPVGs with the same diffraction angle and working wavelength but different diffraction efficiencies. The input and output couplers were then assembled with a glass slab using optical glue (Norland Optical Adhesive 65). The composition of input and output couplers is listed in [Table 4-1](#).

**Table 4-1. Composition of the solutions (by weight).**

Solution	Solute	Solvent	Solute: Solvent
BY solution	Brilliant Yellow	DMF	1:500
Input solution	RM257 (94.75%)	Toluene	~1:2.5
	Irgacure 651 (3.00%)		
	R5011 (2.15%)		
Output solution	RM257 (94.75%)	Toluene	~1:7.0
	Irgacure 651 (3.00%)		
	R5011 (2.15%)		

As shown in [Fig. 4-10\(b\)](#), the input and output gratings are circled in red dashed lines. First, we use a 532-nm laser diode to demonstrate that the incident light can be coupled into the waveguide through CPVG. The light from the laser diode is incident on the input area perpendicular to the glass slab. After being coupled into the waveguide by the input coupler, the light propagates inside the glass slab due to TIR. When entering the output area, the light will be

diffracted out of the glass slab into the observer's eye by the output CPVG. We can clearly see the input light spot, TIR spots, output points, and the leaked light.

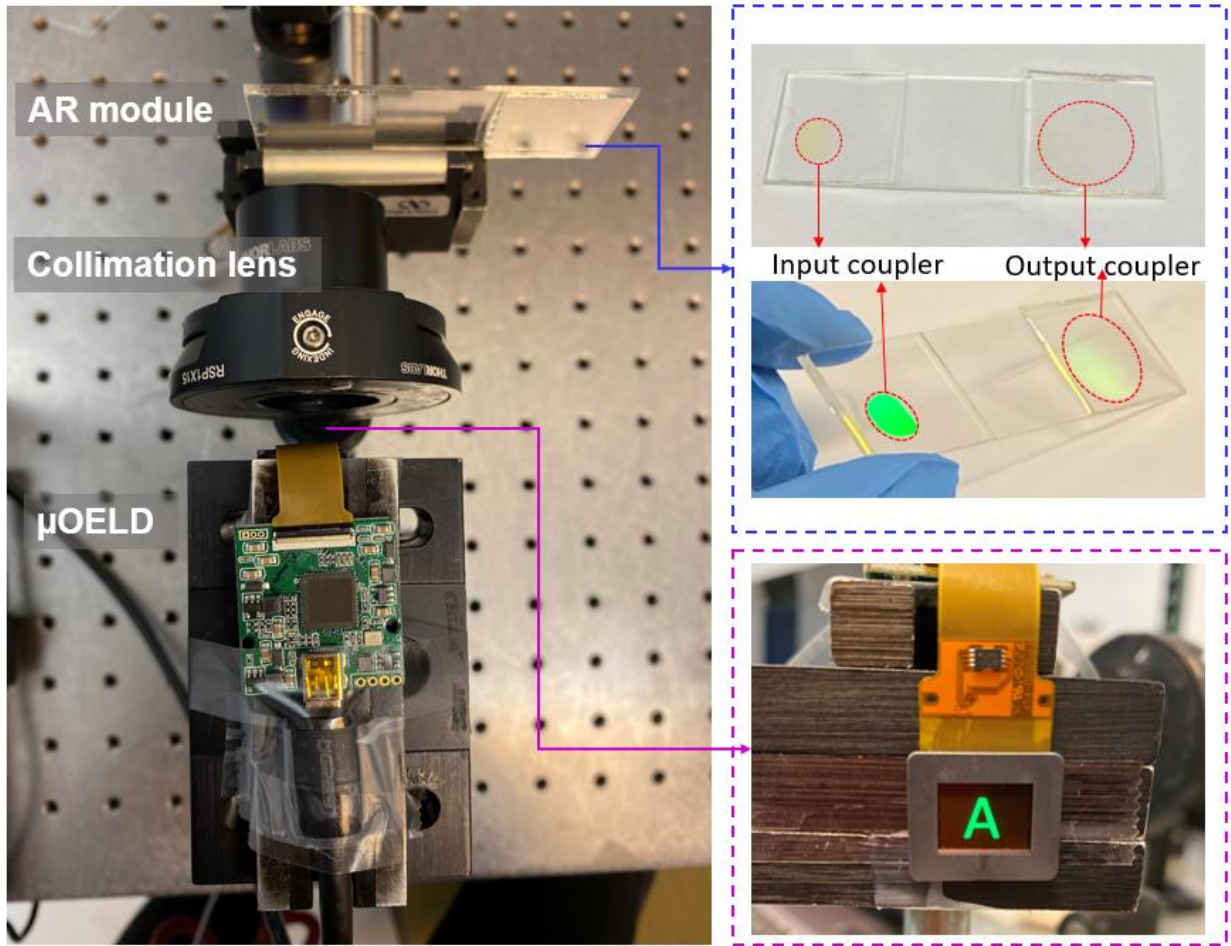


**Figure 4-11** Picture of an AR prototype, including a micro-OLED panel and two CPVGs.

Next, we used a micro-OLED as the image source to build an AR optical system. [Figure 4-11](#) is a picture of our AR prototype. Here we combine a micro-OLED with a lens to generate a collimated input image. [Figure 4-12](#) shows the experimental results. We send a green “A” as the input image into the assembled AR device and then take pictures at the output. The coupled-out image is quite uniform but a little blur. Because when the light propagates in the waveguide (glass

slab), the TIR may occur at or near the edge of the CPVG substrate. The light leakage and scattering at the edge of the glass substrate is circled by blue dashed lines in Fig. 4-10(b). Therefore, the light is scattered by the rough surface of the glass edge. Such a rough edge is caused by our laboratory fabrication equipment and can be eliminated by a better assembly method in the future. Besides, the optical glue that we used to assemble the module will also accumulate at the edge and scatter the light. In general, the results show the feasibility of our CPVG for AR systems. Although the output image is slightly hazy and the background is not bright enough, the prototype still shows good performance.



**Figure 4-12 Picture of an AR prototype, including a micro-OLED panel and two CPVGs.**

#### 4.6 Summary

In this chapter, we experimentally demonstrated CPVGs with an extra-large angular bandwidth while keeping optical efficiency over 80%. This is achieved by inducing gradient pitch along the beam propagation direction. Specifically, our CPVG possesses  $54^\circ$  angular bandwidth,

over 80% average efficiency, and 95% peak efficiency. To make a comparison, we also simulated and fabricated two-layer PVG.

Next, we use this CPVGs to build an AR prototype and demonstrate the feasibility. Due to its wide angular bandwidth, high efficiency, low scattering, high transmittance, and simple fabrication process, our CPVG would be a strong contender for see-through NEDs.

## CHAPTER 5 : GLASSESS-LIKE AR ENABLED BY PVL

### 5.1 Background

In the previous section, we discussed the waveguide-based AR [78-82] achieved by PVGs and CPVGs with high efficiency and enlarged viewing angle. This waveguide design can achieve a large eyebox size with the breaking of Etendue conservation and is therefore the most widely used architecture for current commercial AR devices, such as Microsoft HoloLens, Magic Leap, Wave Optics, and Digi Lens. However, it is worth noting that the waveguide combiners possess a compact design, but the FoV is limited by the constrain of TIR angle.

To provide a realistic viewing experience with a wide FoV, there are two major designs for AR displays aside from waveguide architecture. The freeform optics-based AR can achieve 90° FoV with high image quality [83-85]. However, the freeform optics usually has a large volume with heavyweight and needs sophisticated optical design to eliminate aberrations [86,87]. The other one is free-space combiners-based AR displays [88-90]. This design can achieve a larger FoV and higher optical efficiency compared with waveguide structure. More importantly, it can deliver a glasses-like AR form factor with the capability of true depth imaging. Therefore, the free-space combiners with a sufficient FoV and high degree of design freedom have attracted increasing attention. [Figure 5-1](#) shows the basic structure of glasses-like AR by using a free-space combiner.

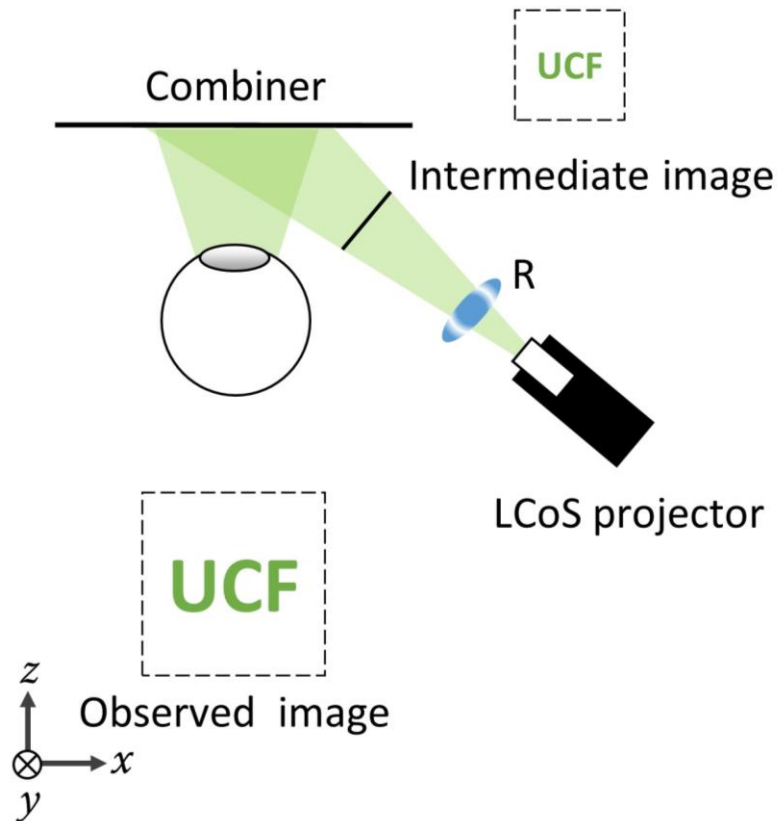


**Figure 5-1 Illustration of a glasses-like AR with LCoS projector.**

In this chapter, we will focus on the glasses-like AR with free-space combiners [91]. Due to different working principles, free-space combiners can be further divided into two categories: reflective and diffractive combiners [92]. Among them, the diffractive free-space combiner with a thin form factor and lightweight is more favorable in the current stage to satisfy the need for glasses-like AR devices.

More specifically, such a diffraction-type free-space combiner is generally realized by holographic optical elements with imaging capability [93]. Based on different system designs, the computer-generated image will be displayed at a designated depth or at infinity. The FoV is dependent on the system design, such as the viewing angle of the combiner lens. To extend the

viewing angle, reducing the  $f$ -number of the combiner lens is an effective and straightforward approach. However, when the  $f$ -number of an off-axis lens is reduced, the imaging aberrations become more serious [93-96]. Therefore, expanding the FoV becomes one of the most pressing challenges in a glasses-like AR system.

PVLs possess several unique properties, such as strong polarization selectivity, large off-axis angle, and simple fabrication process. In addition, liquid crystals exhibit a higher refractive index than conventional photopolymers employed in holographic optical elements. Aside from advances in combiner lens, the optical system design with polarization multiplexing concept has also been proposed with metagratings [97] and successfully implemented in the waveguide-based AR system using polarization gratings [98].

Here, we demonstrate a glasses-like AR system with a novel polarization-dependent combiner (PDC) to expand the FoV. This concept is analogous to the polarization division multiplexing in optical fiber communications, where two orthogonal polarizations are used to double the information capability. Here we extend the viewing angle by presenting the left and right FoVs into two orthogonal polarization states, LCP and RCP light, respectively. The PDC consisting of two PVLs with opposite polarization responses and different off-axis angles is designed to selectively diffract LCP and RCP images. By using an optical engine and a liquid crystal polarization modulator (LCPM) to create two images with orthogonal polarization states, the proposed AR configuration exhibits an extended image content while maintaining a compact form factor.

## 5.2 Polarization Multiplexing

In our system, PDC is a critical optical component, which can distinguish orthogonal polarization states while offering different responses [99]. To meet these requirements, we propose a novel PDC consisting of two PVLs with opposite polarization responses and different diffraction angles. [Figure 5-2\(a\)](#) shows the PVL with a strong polarization selectivity (LCP or RCP) and imaging power. The diffraction angle is denoted as  $\alpha$ . Specifically, the PVL is a patterned CLC device with a designed lens profile. By following the alignment pattern ([Fig. 5-2\(b\)](#)) on the bottom surface, LC molecules continuously and periodically rotate in the  $xy$ -plane and twist along a tilted helical axis ([Fig. 5-2\(c\)](#)) in the  $xz$ -plane. The off-axis angle and focal length of PVL can be controlled by tuning the phase change on surface patterning, which is determined by the interference exposure during fabrication process. As we discussed in Chapter 2, PVLs possess a large diffraction angle and potentially a small  $f$ -number ( $< 1$ ). Besides, PVL is a polymerized ultrathin film (from hundreds of nanometers to several microns) with controllable diffraction efficiency.

To obtain a PDC with two different polarization responses, we stack two PVLs (PVL-L and PVL-R) together. As shown in [Fig. 5-2\(d\)](#), the PVL-R responds to RCP light while PVL-L diffracts the LCP light with a different angle. Due to the thin film form factor of each PVL, the combined PDC can keep an ultrathin profile while increasing functionalities.



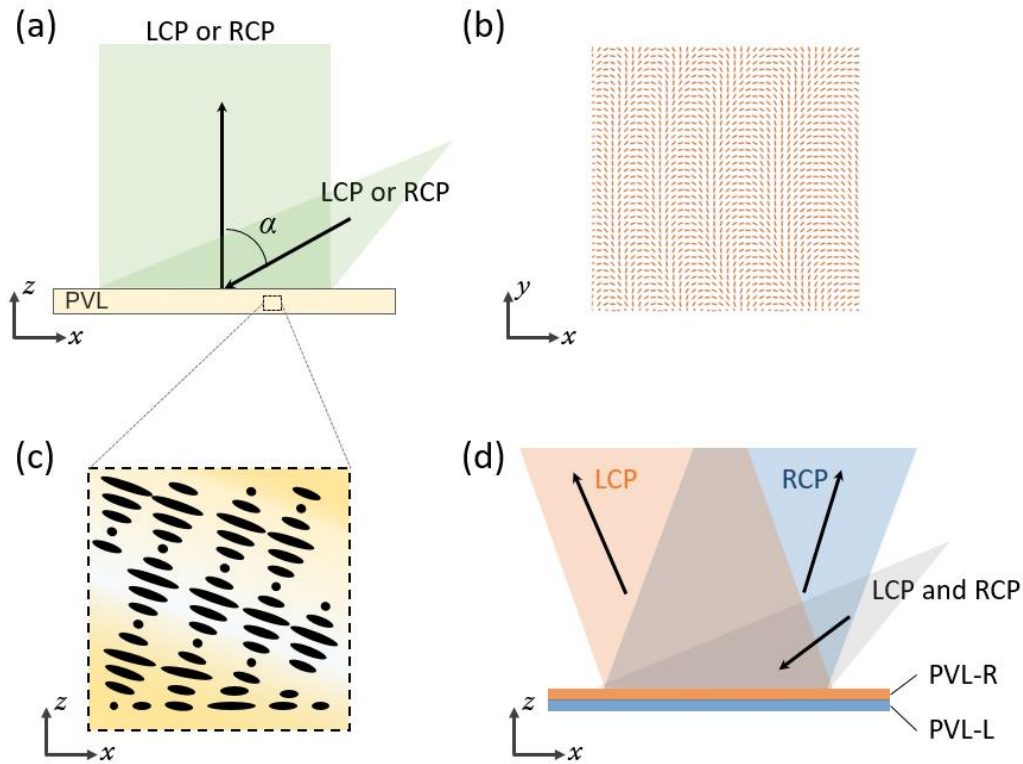


**Figure 5-2 Schematic illustrations of (a) a PVL with (b) surface alignment and (c) CLC structure. (d) Schematic diagram of the PDC with two combined PVLs.**

For a typical free-space AR with a diffractive combiner (Fig. 5-1), the system usually has a pupil-forming design. The image from the light engine is first projected into space with a specific size and depth by the relay optics. Then the intermediate image is delivered to viewer's eye by the diffractive combiner with a designed diopter. The depth and size of the virtual image, which is the observed FoV, can be controlled by changing the distance between the intermediate image and the combiner lens or changing the optical power provided by the combiner. This system is no longer limited by the TIR angle, but the FoV is directly related to the Etendue conservation of a fixed optical system [100-102].

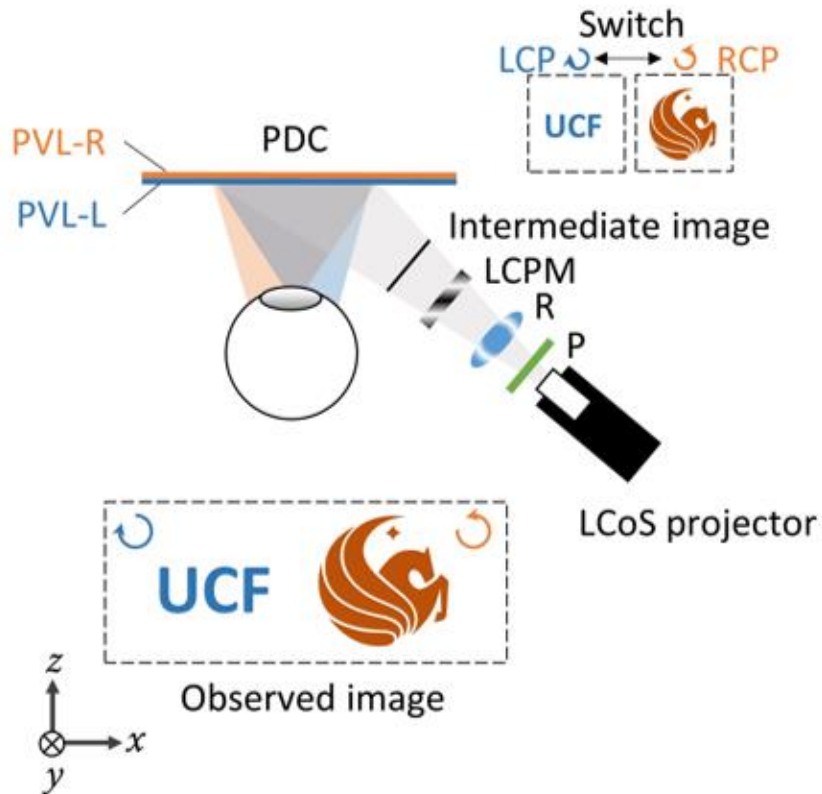


**Figure 5-3 Schematic illustrations of a polarization-time multiplexing free space AR system.** R: relay optics; P: polarizer; LCPM: liquid crystal polarization modular; PDC: polarization-dependent combiner.

To expand the FoV, here we propose a polarization-time multiplexing system based on two orthogonal polarization states to tile the left and right images together. Figure 5-3 depicts the system configuration. The optical engine in the system can be a conventional 2D display, such as a liquid-crystal-on-silicon (LCoS) or a digital light processing (DLP) projector [103-105]. Without losing generality, we add a polarizer in front of the optical engine to make the emitted light with linear polarization in  $xz$ -plane ( $0^\circ$ ). Then an LCPM, aligned after the polarizer, is designed to

obtain modulation between two orthogonal polarization states, namely  $0^\circ$  (in  $xz$ -plane) and  $90^\circ$  (along  $y$ -axis). With an integrated  $\lambda/4$  plate oriented at  $45^\circ$ , these two orthogonal linear polarizations would be converted to LCP and RCP waves, respectively. When switching the computer-generated sub-frame images in the time domain, the LCPM can offer corresponding polarization state for each sub-frame simultaneously. Due to time multiplexing, the final refresh rate of the system should be taken into consideration. Generally, the switching between each sub-frame can be determined by the number of frames, response time of the LCPM, and the frame rate of the LCoS. The response time of LCPM is usually between 1 ms (1 kHz) and 4 ms (250 Hz), depending on the material and cell gap employed. The number of sub-frames is two. Therefore, if the refresh rate of LCoS is 240 Hz, the final system refresh rate will be 120 Hz. Moreover, the tiled image can only be observed when both beams come into the viewer's eye, which means the eyebox should be the overlapping area of the two polarization paths. This area can be further enlarged when the eye relief is decreased, the size of the intermediate image is increased, or the divergence angle of the two paths is reduced.

For example, as shown in [Fig. 5-3](#), when the displayed content is a school logo (Pegasus), the LCPM will be turned on so that it will synchronize the polarization to RCP. When the optical engine switches the content to letters (UCF), then the LCPM will switch the corresponding polarization to LCP. That is to say, the LCPM and the optical engine jointly control the polarization state and content of the intermediate image. However, how to input the intermediate image to the PDC needs to be carefully considered. Let assume the focal length of PVL-L and PVL-R is  $f_L$  and  $f_R$ , respectively, and the angle between the incident beam and the normal direction of the PDC is  $\theta$ . To diffract two images into left and right, the diffraction angle of PVL-L and PVL-R should be

$\theta+\varphi_L$  and  $\theta-\varphi_R$ , respectively. When the intermediate image is placed at a distance  $d_{1-L}$  from PVL-L, the image distance  $d_{2-L}$  can be estimated by the thin lens conjugate equation:

$$d_{2-L} = f_L d_{1-L} / (f_L + d_{1-L}), \quad (5-1)$$

here distance  $d_{2-L}$  is the approximate depth of the observed virtual image from human eye. The size of the virtual image  $A_{2-L}$  should be:

$$A_{2-L} = AM_L = A_1 d_{2-L} / d_{1-L}, \quad (5-2)$$

where  $A_I$  stands for the size of the intermediate image and  $M_L$  is the magnification of the PVL-L. The same goes for the PVL-R. It is worth mentioning that the perceived image depths from two PVLs must be matched to tile the retina image smoothly. Thus, the image distance  $d_{2-L}$  and  $d_{2-R}$  should be the same, namely  $d_2$ , and the  $A_2$  will also be the same. In addition, there can be some space between the two virtual images, but they cannot overlap. Therefore, the overall horizontal FoV can be generally expressed as:

$$FoV = \arctan \left( \frac{A_2}{2d_2} + \tan\varphi_L \right) + \arctan \left( \frac{A_2}{2d_2} + \tan\varphi_R \right) \quad (5-3)$$

If the two images are symmetrically and perfectly tiled without any space, then the horizontal FoV can be simplified as  $FoV=2\arctan (A_2/d_2)$ . The vertical FoV is limited by the viewing angle of each PVL. Generally, the vertical viewing angle is the same as the horizontal one before multiplexing. Therefore, the simplified diagonal FoV can be calculated as  $FoV=\sqrt{5/2} \arctan (A_2/d_2)$ . Based on this equation, if we apply a larger intermediate image, then a wider FoV can be obtained. Moreover, it is worth mentioning that the eyebox should be the overlapping area of the two polarization paths. This area can be further enlarged when the eye relief is decreased, the size of the intermediate image is increased, or the divergence angle of the two paths is reduced.

### 5.3 Experiments

In this section, we show our experimental setup and demonstrate an example for doubling the FoV design discussed above. The system basically follows the proposed layout. In our experiments, a computer-controlled LCoS projector (LG-PH150B) was employed as the optical engine. The PDC consists of two PVLs: PVL-L responding to LCP and PVL-R to RCP, respectively. Generally, the distance between the side image and the combiner is around 3 cm to 5 cm, and the angle between the incident beam and the viewer is around  $30^\circ$  to  $70^\circ$ . Based on the consideration of the real case, for PVL-L, its focal length is  $f_L=3$  cm, off-axis angle is  $52^\circ$ , while for PVL-R its focal length is  $f_R=3$  cm, and off-axis angle is  $27^\circ$ .

Both PVLs were fabricated following the procedure shown in [Fig. 5-4\(a\)](#). First, a thin film of photoalignment material (BY, from Tokyo Chemistry Industry) was spin-coated onto a cleaned glass. Then, the substrates with BY coating were mounted on the exposure setup to record the surface alignment patterns. After exposure, the liquid crystal mixture (LCM) with opposite chiral dopant, R5011 and S5011, was spin-coated for the PVL-L and PVL-R, respectively. Finally, the samples were polymerized by a UV lamp. More detailed operation principles and fabrication procedures of the PVL can be found in [15,24].

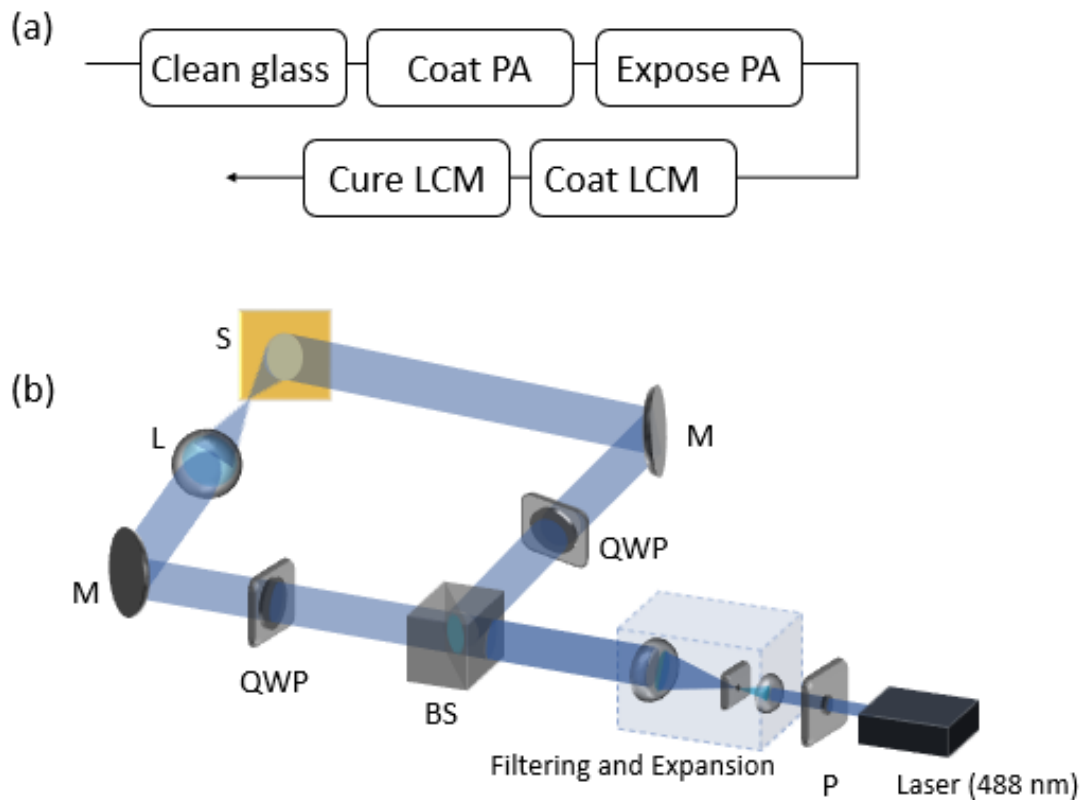


**Figure 5-4 (a) PVL fabrication workflow. (b) Exposure setup for recording the surface pattern.** (PAL: photoalignment layer; LCM: liquid crystal mixture; P: polarizer; SLM: spatial light modulator; QWP: quarter-wave plate; L: template lens; S: sample).

Figure 5-5(a) shows a photo of the fabricated PVL-R, which is circled by the white dashed lines and the lens surface is clear and uniform. The green images observed are the ceiling fluorescent lamps in our lab. The other colors are the dispersion from this diffractive lens. Next, we fabricated PVL-L and laminated it with PVL-R together using a UV optical glue (NOA65), as Fig. 5-5(b) shows. The PDC region is circled by the white dashed lines. The thickness of each PVL is  $\sim 1 \mu\text{m}$ , and the total thickness of PDC, including the substrates, is 1 mm. The text shown in Fig. 5-5(c) is imaged through the sample. The distance between PDC and camera is 5 cm, and the target

is 7 cm away. The clear image seen through the PDC region indicates the combiner exhibits a relatively high transmittance and negligible scattering. Due to the color of the employed photoalignment material (BY), the sample appears yellowish, but this can be eliminated by using a colorless photo-alignment material.

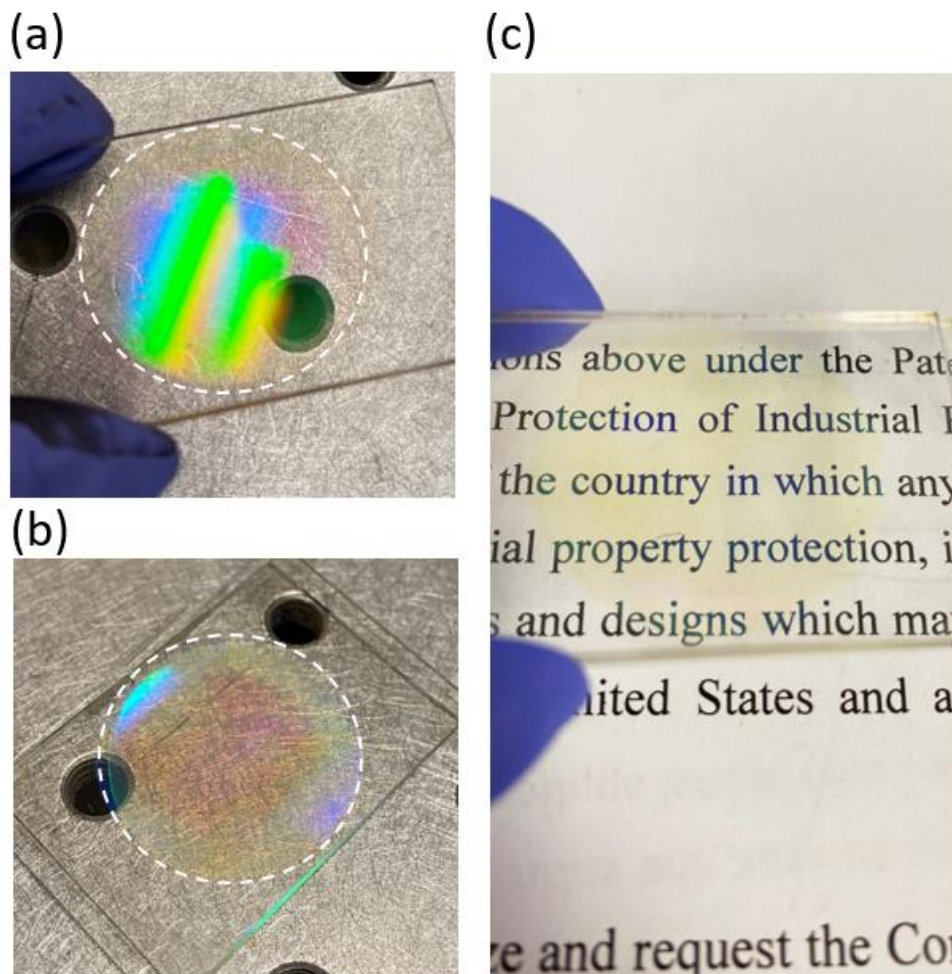


**Figure 5-5** Photo of (a) the fabricated PVL-L and (b) the PDC consisting of PVL-L and PVL-R. (c) A photo taken through the PDC sample, where the PDC region is yellowish. The distance between PDC and camera is 5 cm, and the target is 7 cm away.

To prepare the LCPM, we filled a liquid crystal (MLC-6686, Merck) into a commercial twisted nematic (TN) cell [106-108] (cell gap  $d=4.9 \mu\text{m}$ ) and an AC voltage is applied to control

the on and off states. Normally, the voltage is 5 Vrms, depending on the employed LC material and cell gap. Then we used a broadband quarter-wave plate to convert the linearly polarized light into circularly polarized light. The whole experimental setup was constructed on an optical table. As captured in Fig. 5-6, a positive lens with focal length  $f = 12$  cm was used as the relay optics in our experiments. A camera was placed in front of the PDC to capture the displayed images. To eliminate the ghost images generated by the dispersion from diffractive optics, we added a notch filter after the polarizer.

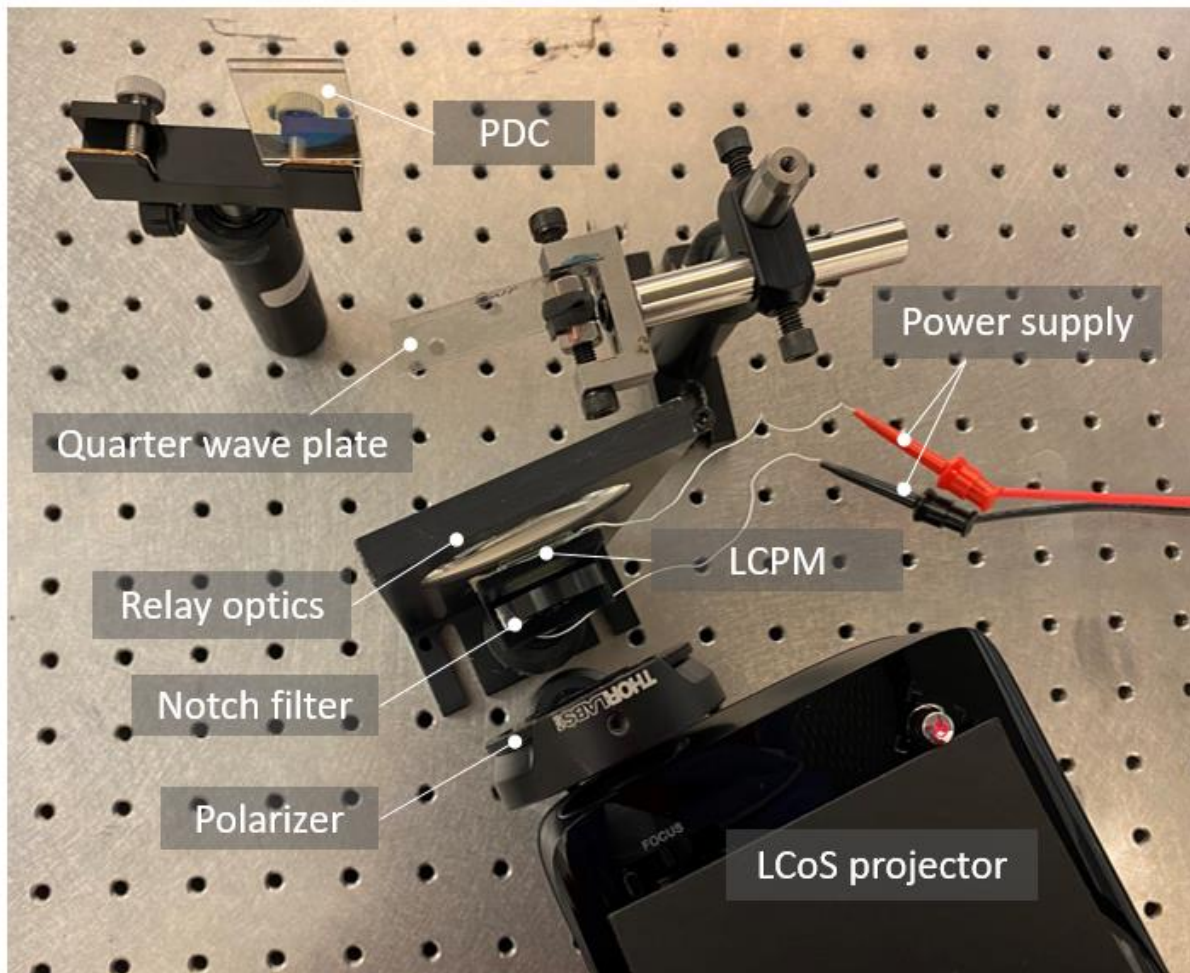


**Figure 5-6 Schematic illustration of the experiment setup.**



Figure 5-7 shows the experimental results. The intermediate image is 2.9 cm away from the PDC. The angle between the input beam and the normal of the PDC is about  $40^\circ$ . When we turn the LCPM on, there will be only LCP light. The viewing angle of LCP alone is about  $26^\circ$  with showing UCF letters, as illustrated in Fig. 5-7(a). Due to the large off-axis imaging, we can see the obvious distortion, especially for the letter U. This optical aberration can be mitigated through pre-processing the input contents, but this will bring more burdens to both computation and information transforms. By switching the LCPM from on to off state, we can observe the RCP image. As depicted in Fig. 5-7(b), the viewing angle is  $23^\circ$  with showing school logo. Then we simultaneously switch the LCPM and the computer-generated images to observe the combined image.

As expected, in Fig. 5-7(c), the observed overall horizontal FoV is the combination of RCP and LCP light, extended from  $\sim 25^\circ$  (sub-FoV) to  $\sim 50^\circ$  (tiled FoV). Besides, the PDC's diffraction efficiency for LCP mode is slightly lower than that for RCP. This issue can be solved by controlling the film thickness for each polarization channel or pre-image processing compensation on the computer side.

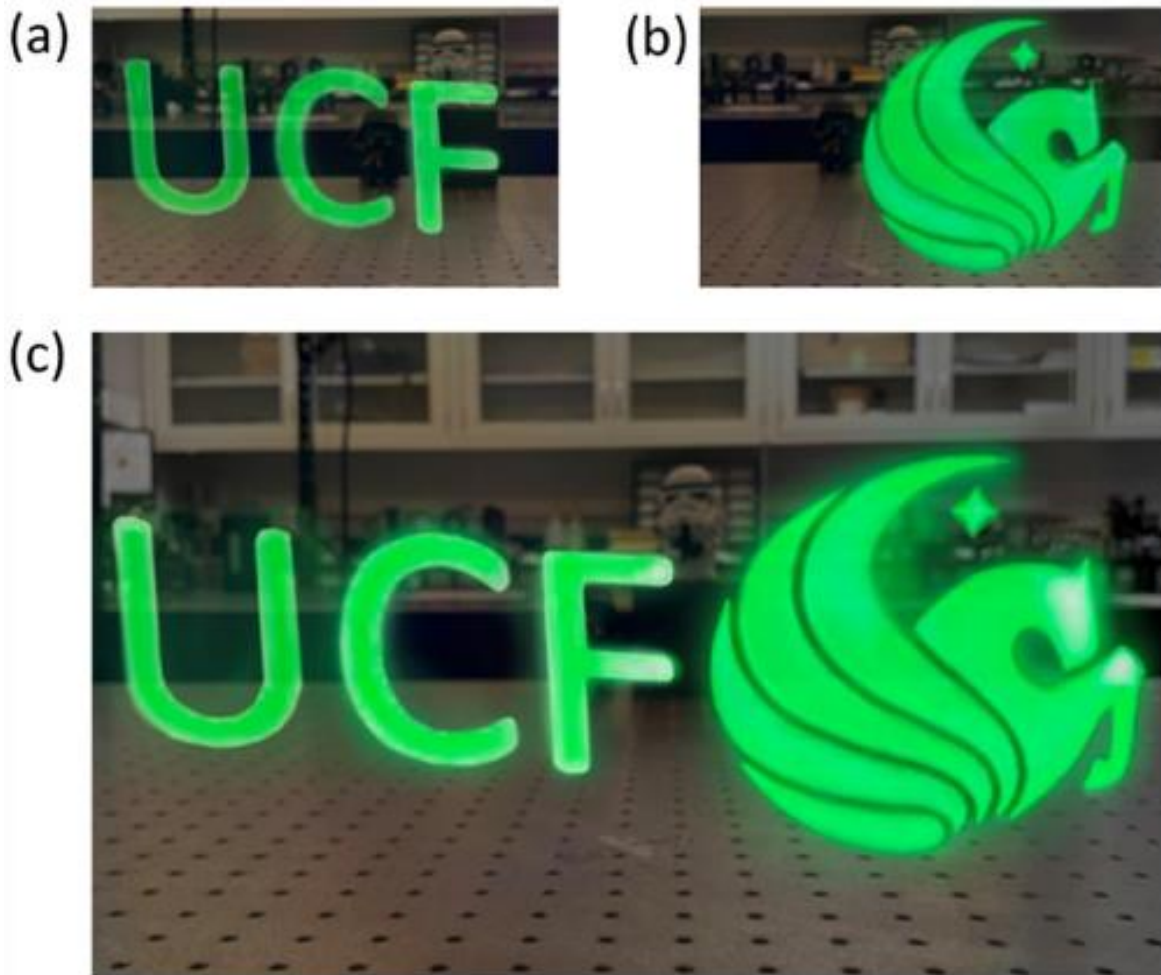


**Figure 5-7 (a) Captured image of LCP light, UCF. (b) Captured image of RCP, school logo. (c) Captured image of the combined images.**

In our demonstration, we use a novel PDC with two opposite polarization responses to achieve an extended FoV. In order to further improve the functionality based on the polarization-time multiplexing system, the number of sub-frames and the PDC can be optimized.

Firstly, this proposed system is a monochromatic design for the green light. However, one of the current requirements for AR displays is a full-color image. To achieve this, we need to stack

three layers of PDC for red, green, and blue, respectively. It is worth mentioning that the diffractive PDC suffers from severe dispersion. To display full-color image with the stacked PDC, a narrow band image source is necessary. Figure 5-8 shows the full-color system design achieved by a color wheel [109]. This approach can easily solve the dispersion issue; however, the disadvantage is the loss of frame rate.

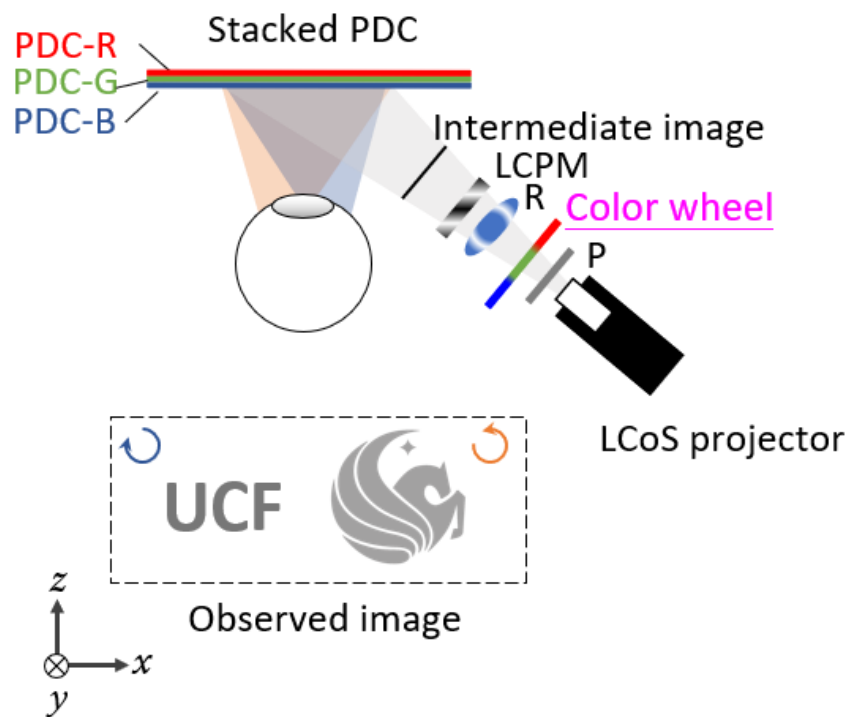


**Figure 5-8 Schematic illustration of full-color system design with color wheel.**

Secondly, the system is not limited to horizontally expand FoV. In our proposed system, although there are only two orthogonal polarization states, the number of image channels can be further increased without being limited by the number of orthogonal polarizations. As depicted in Fig. 5-9(a), the image contents can be encoded into more than  $N$  channels ( $N \geq 3$ ) with the help of an improved PDC composed of active half-wave plates (HWPs) and PVLs. Each active HWP can be switched between on and off states to provide PVLs with the corresponding polarized light.

Due to the requirement of single-polarization incidence, the LCPM can be simplified as a QWP to offer LCP or RCP light.

More specifically, as an example illustrated in [Fig. 5-9\(b\)](#), when an incident light is RCP, the first HWP is turned on to convert RCP to LCP. The LCP light is diffracted by the first PVL-L. The image content is delivered to the viewer's eye. If the first HWP keeps at off state with the RCP incidence, the light will pass through the HWP and the first PVL-L, then encounter the second HWP with on state. The RCP will be converted to LCP and diffracted by the second PVL-L with a different diffraction angle. By analogy, PVLs of different angles can be stacked layer by layer. [Figure 5-9\(c\)](#) illustrates the image from each PVL with different diffraction angles. Moreover, this multiplexing system can be applied to expanding the vertical FoV as well. The image content can be encoded and then tiled in  $xy$ -plane instead of only along  $x$ -axis. To accommodate a large incident angle, a phase compensation film is usually required to keep the HWP working properly. Otherwise, multiple ghost images could be observed. Moreover, if the LCP light is not completely diffracted by the working PVL-L, then the remaining light will be further imaged by the following PVLs, which in turn generates ghost images. To overcome this issue, the HWP behind the working PVL-L can be turned on to convert the LCP light back to RCP.

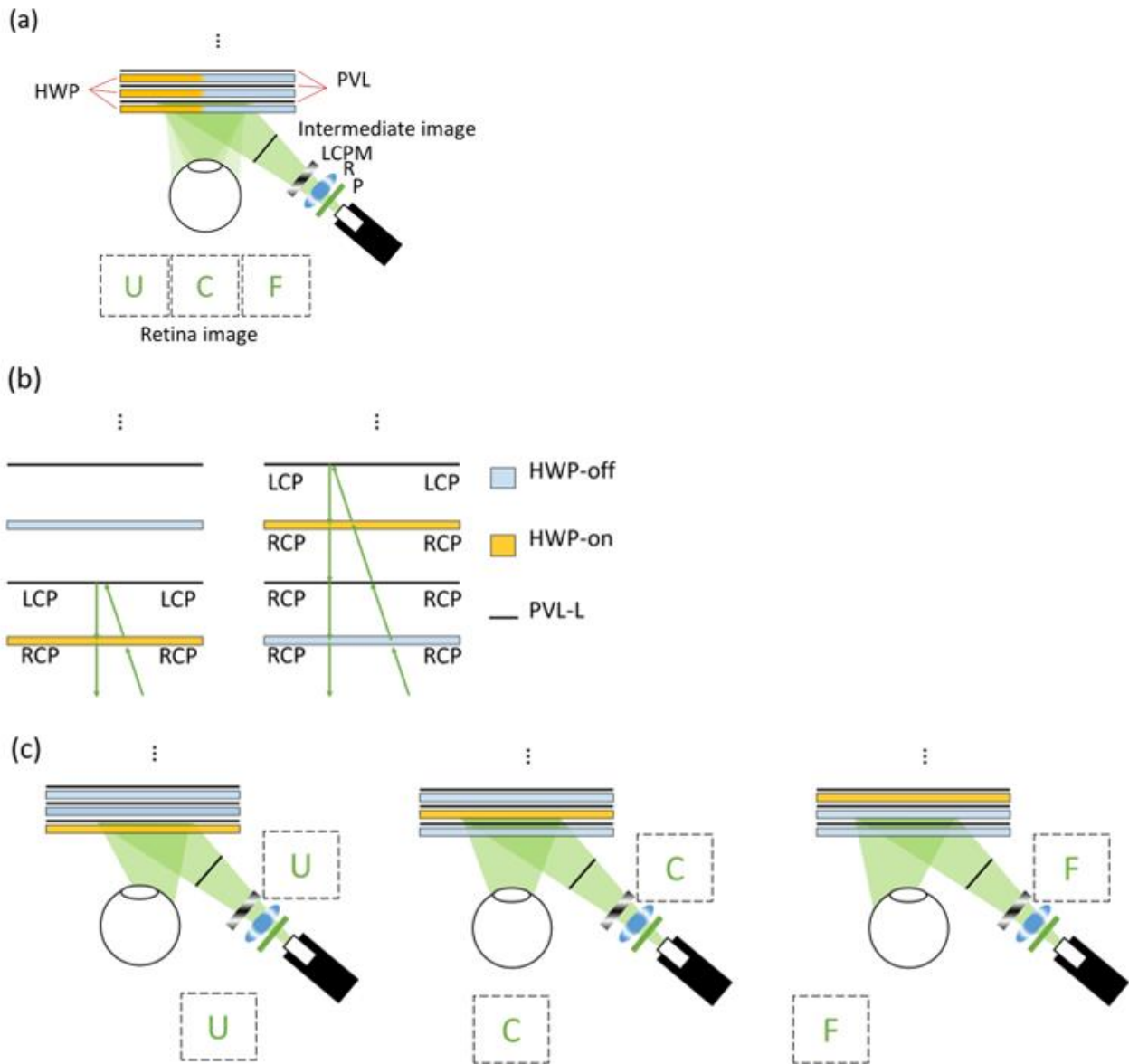


**Figure 5-9 Schematic illustrations of (a) an improved polarization-time multiplexing AR system with (b) a PDC composed of active HWP and PVLs. (c) Schematic illustrations of the image from each PVL. (HWP: half-wave plate; R: relay optics; P: polarizer; LCPM: liquid crystal polarization modular; PDC: polarization-dependent combiner)**

#### 5.4 Summary

In this chapter, we proposed and demonstrated a polarization-time multiplexing system to double the FoV of a glasses-like AR display. The multiplexing is achieved by PDC, which is composed of two PVLs with orthogonal polarization responses. In experiment, a PVL is fabricated by patterning CLC, which can achieve high uniformity, large diffraction angle, and negligible scattering. By constructing the proposed system with an electronically controlled LCPM, the enlarged overall horizontal is achieved.

To further improve the system, we proposed a full-color system by using color wheel. Then we optimized the PDC with active HWPs. By stacking the layer of active HWPs and PVLs, we can theoretically obtain an ultra-wide FoV by tiling multiple sub-frame images based on the polarization-time multiplexing system. In summary, we presented a promising approach to achieving wide FoV in glasses-like AR displays while keeping a simple system configuration.

## CHAPTER 6 : CONCLUSIONS

Augmented reality and virtual reality are fascinating technologies and generate various impactful applications that can reshape human lives. In this dissertation, we contribute novel patterned LC devices to enhance the performance of near-eye displays, aimed at making augmented reality and virtual reality even better.

The patterned LC devices can be divided into three parts based on the dimension of the surface pattern. For zero-dimension, we emphasize the CLC reflector with homogeneous alignment, Bragg reflection, and strong polarization selectivity. Based on this device, we proposed and demonstrated a foveated imaging design to enhance resolution for the VR system. A dramatic resolution improvement (4.4 times) has been demonstrated with a compact form factor. The essence of this design is optically splitting images into two different optical paths, making use of the polarization selective nature of the CLC reflector.

For one dimension, we focus on the CLC grating, also called polarization volume grating, with linearly changed alignment, large diffraction angle, and nearly 100% diffraction efficiency. Based on polarization volume grating, we proposed a polarization volume grating-based waveguide AR system with high system efficiency. Furthermore, to obtain a larger field of view, we optimized the LC structure inside the polarization volume grating and induced gradient pitch in the vertical direction. By gradually changing the pitch length from the bottom to the top, the angular response of polarization volume grating can be enlarged three times while keeping a high efficiency and large diffraction angle. This gradient-pitch grating is also called chirped polarization volume grating. Furthermore, we applied this chirped polarization volume grating into the

waveguide-based augmented reality system to enlarge the viewing angle for better imaging performance.

For two-dimension, we introduced the C LC lens, also called polarization volume lens, with parabolically changed alignment and large diffraction angle. Since the polarization volume lens can achieve off-axis imaging with the ultrathin format factor, it becomes a perfect candidate as the optical combiner for the glasses-like augmented reality displays. Based on the polarization volume lens, we propose a novel glasses-like AR system design. Combining the polarization multiplexing and time multiplexing, to extend the field of view without inducing extra volume. The core of the system is the polarization multiplexing images with a single image source. Thanks to the nature of patterned CLC devices with strong polarization selectivity, we can tile two separated images with orthogonal polarization states thereby doubling the field of view in the horizontal direction.

With all the efforts, we expect patterned LC devices with different features to bring a new dawn to LC-based photonics and make more contributions as a useful technology for next-generation near-eye displays, enabling augmented and virtual reality become practical applications.



## **APPENDIX: STUDENT PUBLICATIONS**

### Journal Publications

- [1] K. Yin, E. L. Hsiang, J. Zou, Y. Li, Z. Yang, Q. Yang, P. C. Lai, C. L. Lin, and S. T. Wu, “Advanced liquid crystal photonics for virtual reality and augmented displays: Principles and Applications,” *Light Sci. Appl* (Under review).
- [2] K. Yin, Z. He, Y. Li, and S. T. Wu, “Novel polarization-dependent combiner for wide field-of-view glass-like near-eye displays,” *J. Soc. Inf. Display* (Accepted).
- [3] Y. Li, Q. Yang, J. Xiong, K. Yin, and S. T. Wu, “3D displays in augmented and virtual realities with holographic optical elements,” *Opt. Express* 29(26), 42696-42712 (2021).
- [4] Z. He, K. Yin, and S. T. Wu, “Miniature planar telescopes for efficient, wide-angle, high-precision beam steering,” *Light Sci. Appl* 10, 134 (2021).
- [5] K. Yin, Z. He, J. Xiong, J. Zou, K. Li, and S. T. Wu, “Virtual Reality and Augmented Reality Displays: Advances and Future Perspectives,” *J. Phys. Photonics* 3, 022010 (2021).
- [6] K. Yin, Z. He, K. Li, and S. T. Wu, “Doubling the FOV of AR displays with a liquid crystal polarization-dependent combiner,” *Opt. Express* 29, 11512-11519 (2021).
- [7] K. Yin, Z. He, K. Li, and S. T. Wu, “Novel polarization-dependent combiner for wide field-of-view glass-like near-eye displays,” *J. Soc. Inf. Display* 29, 311-317 (2021).
- [8] Z. He, K. Yin, K.H. Fan-Chiang, and S. T. Wu, “Enlarging the Eyebox of Maxwellian Displays with a Customized Liquid Crystal Dammann Grating,” *Crystals* 11, 195 (2021).
- [9] J. Zou, Z. He, Q. Yang, K. Yin, K. Li, and S. T. Wu, “Large-angle two-dimensional grating with hybrid mechanisms,” *Opt. Lett.* 46, 920-923 (2021).
- [10] Z. He, K. Yin, and S. T. Wu, “Peculiar polarization response in chiral liquid crystal stacks for multispectral camouflage,” *Opt. Express* 29, 2931-2939 (2021).

- [11] K. Yin, J. Xiong, Z. He, and S. T. Wu, "Patterning Liquid Crystal Alignment for Ultra-Thin Flat Optics," ACS Omega 5, 31485-31489 (2020).
- [12] J. Xiong, K. Yin, K. Li, and S. T. Wu, "Holographic optical elements for augmented reality: principles, present status, and future perspectives," Advanced Photonics Research 2, 2000049 (2020).
- [13] T. Zhan, K. Yin, J. Xiong, Z. He, and S. T. Wu, "Augmented reality and virtual reality: perspectives and challenges," iScience 23, 101397 (2020).
- [14] J. Zou, E. L. Hsiang, T. Zhan, K. Yin, Z. He, and S. T. Wu, "High Dynamic Range Head-up Display," Opt. Express 28, 24298-24307 (2020).
- [15] Z. He, K. Yin, and S. T. Wu, "Standing wave polarization holography for realizing liquid crystal Pancharatnum-Berry phase lenses," Opt. Express 28, 21729-21736 (2020).
- [16] K. Yin, T. Zhan, J. Xiong, Z. He, and S. T. Wu, "Polarization Volume Gratings for Near-eye Displays and Novel Photonic Devices," Crystals 10, 561 (2020).
- [17] K. Yin, Ziqian He, and S. T. Wu, "Reflective polarization volume lens with small F-number and large diffraction angle," Adv. Opt. Mater. 8, 2000170 (2020).
- [18] Z. He, K. Yin, E. L. Xiang, and S. T. Wu, "Birefringent light-shaping films for mini-LED backlights," J. Soc. Inf. Disp. 28, 476-482 (2020).
- [19] K. Yin, H. Y. Lin, and S. T. Wu, "Chirped polarization volume grating for wide FOV and high efficiency waveguide-based AR displays," J. Soc. Inf. Disp. 28, 368-374 (2020).
- [20] Z. He, K. Yin, and S. T. Wu, "Passive polymer-dispersed liquid crystal enabled multi-focal plane displays," Opt. Express 28, 15294 (2020).

- [21] Z. He, K. Yin, E.L. Hsiang and S. T. Wu, "Volumetric light-shaping polymer-dispersed liquid crystal films for mini-LED backlights," *Liq. Cryst.* 47, 1458-1463 (2020).
- [22] K. Yin, H. Y. Lin, and S. T. Wu, "Chirped polarization volume grating with ultra-wide angular bandwidth and high efficiency for see-through near-eye displays," *Opt. Express* 27, 35895-35902 (2019).
- [23] Z. He, G. Gou, R. Chen, K. Yin, T. Zhan, and S. T. Wu, "Liquid Crystal Beam Steering Devices: Principles, Recent Advances, and Future Developments," *Crystals* 9, 292 (2019).
- [24] K. Yin, Y. H. Lee, Z. He, and S. T. Wu, "Stretchable, flexible, and adherable polarization volume grating film for waveguide-based augmented reality displays," *J. SID* 27, 232-237 (2019).
- [25] T. Zhan, Y. H. Lee, J. Xiong, G. Tan, K. Yin, J. Yang, S. Liu, and S. T. Wu, "High-efficiency switchable optical elements for advanced head-up displays," *J. SID* 27 223-231 (2019).
- [26] K. Yin, Y. H. Lee, Z. He, and S. T. Wu, "Stretchable, flexible, rollable, and adherable polarization volume grating film," *Opt. Express* 27, 5814-5823 (2019).
- [27] R. Chen, Y. H. Lee, T. Zhan, K. Yin, Z. An, and S. T. Wu, "Multi-stimuli-responsive self-organized liquid crystal Bragg gratings," *Adv. Opt. Mater.* 7, 1900101 (2019).
- [28] T. Zhan, Y. H. Lee, G. Tan, J. Xiong, K. Yin, F. Gou, J. Zou, N. Zhang, D. Zhao, J. Yang, S. Liu, and S. T. Wu, "Pancharatnam-Berry optical elements for head-up and near-eye displays," *J. Opt. Soc. Am. B* 36, D52-D65 (2019).
- [29] Y. H. Lee, G. Tan, K. Yin, T. Zhan, and S. T. Wu, "Compact see-through near-eye display with depth adaption," *J. SID* 26, 64-70 (2018).

- [30] Y. H. Lee, K. Yin, and S. T. Wu, “Reflective polarization volume gratings for high efficiency waveguide-coupling augmented reality displays,” *Opt. Express* 25, 27008-27014 (2017).

### Conference Proceedings

- [1] K. Yin, Z. He, L. Li, and S. T. Wu, "Foveated imaging by polarization multiplexing for compact near-eye displays," SID Symp. Digest (Accepted Oral, May 2022).
- [2] K. Yin, Z. He, K. Li, and S. T. Wu, "Polarization-dependent combiner for wide field-of-view glasses-Like AR Displays," Optical Architectures for Displays and Sensing in Augmented, Virtual, and Mixed Reality (AR, VR, MR) III Proc. SPIE 11931, 11931J (2022).
- [3] K. Yin, T. Zhan, J. Xiong, Z. He, K. Li, S. T. Wu, "Liquid crystal polarization volume gratings for near-eye displays," Advances in Display Technologies XI, Proc. SPIE 11708, 1170804 (2021).
- [4] K. Yin, Z. He, K. Li, and S. T. Wu, "Novel Polarization-Dependent Combiner for Wide Field-of-View Glasses-Like AR Displays," SID Symp. Digest 52,417-420 (Accepted Oral, May 2021).
- [5] J. Zou, E. L. Hsiang, T. Zhan, K. Yin, Z. He, and S. T. Wu, "High-Dynamic-Range HUD with a Polarization Selective Optical Combiner," SID Symp. Digest 52, 564-567 (Accepted Oral, May 2021).
- [6] Z. He, K. Yin, K.H. Fan-Chiang, and S. T. Wu, "Optimized Liquid-Crystal Dammann Grating for Eyebow Expansion in Maxwellian-View Displays," SID Symp. Digest 52, 431-434 (Accepted Oral, May 2021).
- [7] K. Yin, Z. He, and S. T. Wu, "Spotlighting Recent Advances in Liquid-Crystal Devices for Beam-Steering Applications," Information Display (January/February) 9-13 (2021).

- [8] K. Yin, H. Y. Lin, Z. He, and S. T. Wu, “Chirped polarization volume grating for wide FOV and high efficiency waveguide-based AR displays,” SID Symp. Digest 51, 371 (Accepted Oral, May 2020).
- [9] J Xiong, G Tan, K Yin, T Zhan, and S. T. Wu, “A Scanning Waveguide Display with 100° of FOV,” SID Symp. Digest 51, 583 (Accepted Oral, May 2020).
- [10] Z. He, K Yin, E. L. Hsiang, M. C. Li, S. L. Lee, K. C. Tien, and S. T. Wu, “Birefringent Light-Shaping Film for Mini-LED Backlights,” SID Symp. Digest 51, 239 (Accepted Oral, May 2020, San Jose, California).
- [11] K. Yin, Y. H. Lee, Z. He, and S. T. Wu, “Stretchable, flexible, and adherable polarization volume grating film for waveguide-based augmented reality displays,” SID Symp. Digest 50, 676 (Accepted Oral, May 2019, San Jose, California).
- [12] T. Zhan, Y. H. Lee, J. Xiong, G. Tan, K. Yin, J. Yang, S. Liu, and S. T. Wu, “High-efficiency switchable optical elements for advanced head-up displays,” SID Symp. Digest 50, 830 (Accepted Oral, May 2019, San Jose, California).
- [13] R. Chen, Y. H. Lee, T. Zhan, K. Yin, Z. An, and S. T. Wu, “Fast-Response Polarization Volume Gratings for AR/VR Displays” SID Symp. Digest 50, 838 (Accepted Oral, May 2019, San Jose, California).
- [14] Z. He, Y. H. Lee, K. Yin, and S. T. Wu, “Recent advances in liquid-crystal polarization volume gratings,” Liquid Crystals XXIII Proc. SPIE 11092, 1109204 (29 August 2019).
- [15] K. Yin, Y. H. Lee, and S. T. Wu, “High Efficiency Polarization Volume Grating for Waveguide-based AR Displays,” SID Symp. Digest 49, 208 (Accepted Oral, May 2018, Los Angeles, California).

- [16] Y. H. Lee, G. Tan, K. Yin, T. Zhan, and S. T. Wu, “Compact See-through Near-eye Display with Depth Adaption,” SID Symp. Digest 49, 1060 (Accepted Oral, May 2018, Los Angeles, California).



## REFERENCES

- [1] K. Yin, Z. He, J. Xiong, J. Zou, K. Li, and S. T. Wu, “Virtual Reality and Augmented Reality Displays: Advances and Future Perspectives,” *J. Phys. Photonics* 3, 022010 (2021).
- [2] B. C. Kress, *Optical Architectures for Augmented-, Virtual-, and Mixed-Reality Headsets*. (Bellingham: SPIE Press, 2020).
- [3] I. E. Sutherland, “A head-mounted three-dimensional display,” *Proc. FJCC* 1, 757–64 (1968).
- [4] S. S. Fisher, M. McGreevy, J. Humphries, and W. Robinett, “Virtual environment display system,” *Proc. 1986 Workshop on Interactive 3D Graphics* 77–87 (1987).
- [5] Y. Amitai, A. A. Friesem, and V. Weiss, “Holographic elements with high efficiency and low aberrations for helmet displays,” *Appl. Opt.* 28, 3405–16 (1989).
- [6] B. Lee, “Review of the present status of optical fiber sensors,” *Opt. Fiber Technol.* 9, 57–79 (2003).
- [7] D. Lin, P. Fan, E. Hasman, and M. L. Brongersma, “Dielectric gradient metasurface optical elements,” *Science* 345, 298–302 (2014).
- [8] W. T. Chen, A. Y. Zhu, V. Sanjeev, M. Khorasaninejad, Z. Shi, E. Lee, and F. Capasso, “A broadband achromatic metalens for focusing and imaging in the visible,” *Nat. Nanotechnol.* 13, 220–226 (2018).
- [9] H. Chen, J. H. Lee, B. Y. Lin, S. Chen, and S. T. Wu, “Liquid crystal display and organic light-emitting diode display: present status and future perspectives,” *Light Sci. Appl.* 7, 17168 (2018).
- [10] R. C. Schank, *Conceptual Information Processing*. (New York: Elsevier, 2014)

- [11] T. Zhan, K. Yin, J. Xiong, Z. He, and S. T. Wu, “Augmented reality and virtual reality: perspectives and challenges,” *iScience* 23, 101397 (2020).
- [12] J. Xiong, E. L. Hsiang, Z. He, T. Zhan, and S. T. Wu, “Augmented reality and virtual reality displays: emerging technologies and future perspectives,” *Light Sci. & Appl.* 10, 216 (2021).
- [13] B. Wheelwright, Y. Sulai, Y. Geng, S. Luanava, S. Choi, W. Gao, and J. Gollier, “Field of view: not just a number,” *Proc. SPIE* 10676, 1067604(2018).
- [14] C. A. Curcio, K. R. Sloan, R. E. Kalina, and A. E. Hendrickson, “Human photoreceptor topography,” *J. Comp. Neurol.* 292, 497–523 (1990).
- [15] K. Yin, J. Xiong, Z. He, and S. T. Wu, “Patterning Liquid Crystal Alignment for Ultra-Thin Flat Optics,” *ACS Omega* 5, 31485-31489 (2020).
- [16] J. Xiong, K. Yin, K. Li, S. T. Wu, “Holographic optical elements for augmented reality: principles, present status, and future perspectives,” *Adv. Photonics Res.* 2, 2000049 (2021).
- [17] N. V. Tabiryan, S. V. Serak, D. E. Roberts, D. M. Steeves, and B. R. Kimball, “Thin waveplate lenses of switchable focal length—new generation in optics,” *Opt. Express* 23, 25783-25794 (2015).
- [18] N. V. Tabiryan, D. E. Roberts, Z. Liao, J. Y. Hwang, M. Moran, O. Ouskova, A. Pshenichnyi, J. Sigley, A. Tabirian, R. Vergara, and L. De Sio, “Advances in transparent planar optics: enabling large aperture. Ultrathin Lenses,” *Adv. Opt. Mater.* 9, 2001692 (2021).

- [19] T. Zhan, Y. H. Lee, G. Tan, J. Xiong, K. Yin, F. Gou, J. Zou, N. Zhang, D. Zhao, J. Yang, S. Liu, and S. T. Wu, "Pancharatnam-Berry optical elements for head-up and near-eye displays," *J. Opt. Soc. America B*, 36, D52-D65 (2019).
- [20] V. Chigrinov, V. M. Kozenkov, and H.-S. Kwok, *Photoalignment of Liquid Crystalline Materials: Physics and Applications*. (John Wiley & Sons, 2008).
- [21] M. Schadt, K. Schmitt, V. Kozinkov, and V. Chigrinov, "Surface-Induced Parallel Alignment of Liquid Crystals by Linearly Polymerized Photopolymers," *Jpn. J. Appl. Phys.* 31, 2155 (1992).
- [22] G. Tan, Y. H. Lee, F. Gou, M. Hu, Y. F. Lan, C. Y. Tsai, and S. T. Wu, "Macroscopic model for analyzing the electro-optics of uniform lying helix cholesteric liquid crystals," *J. Appl. Phys.* 121, 173102 (2017).
- [23] L. Li, D. Bryant, and P. J. Bos, "Liquid crystal lens with concentric electrodes and inter-electrode resistors," *Liq. Cryst. Rev.* 2, 130–154 (2014).
- [24] K. Yin, Z. He, and S. T. Wu, "Reflective Polarization Volume Lens with Small  $f$ -Number and Large Diffraction Angle," *Adv. Opt. Mater.* 8, 2000170 (2020).
- [25] S. C. McEldowney, D. M. Shemo, R. A. Chipman, and P. K. Smith, "Creating vortex retarders using photoaligned liquid crystal polymers," *Opt. Lett.* 33, 134-136 (2008).
- [26] D. Mawet, E. Serabyn, K. Liewer, C. Hanot, S. McEldowney, D. Shemo, and N. O'Brien, "Optical vectorial vortex coronagraphs using liquid crystal polymers: theory, manufacturing and laboratory demonstration," *Opt. Express* 17, 1902-1918 (2009).
- [27] S. R. Nersisyan, N. V. Tabiryan, D. Mawet, and E. Serabyn, "Improving vector vortex waveplates for high-contrast coronagraphy," *Opt. Express* 21, 8205-8213 (2013).

- [28] S. Slussarenko, S. Murauski, T. Du, V. Chigrinov, L. Marrucci, and E. Santamato, “Tunable liquid crystal q-plates with arbitrary topological charge,” *Opt. Express* 19, 4085-4090 (2011).
- [29] J. Kobashi, H. Yoshida, M. Ozaki, “Planar optics with patterned chiral liquid crystals,” *Nature Photonics* 10, 389-92 (2016).
- [30] Y. Weng, D. Xu, Y. Zhang, X. Li, and S. T. Wu, “A polarization volume grating with high efficiency and large diffraction angle,” *Opt. Express* 24, 17746-17759 (2016).
- [31] Y. H. Lee, K. Yin, and S. T. Wu, “Reflective polarization volume gratings for high efficiency waveguide-coupling augmented reality displays,” *Opt. Express* 25, 27008-27014 (2017).
- [32] C. Oh and M. J. Escuti, “Achromatic diffraction from polarization gratings with high efficiency,” *Opt. Lett.* 33, 2287–2289 (2008).
- [33] H. Sarkissian, B. Park, N. Tabirian, B. Zeldovich, “Periodically aligned liquid crystal: potential application for projection displays,” *Mol. Cryst. Liq. Cryst.* 451, 1–19 (2006).
- [34] J. Xiong, R. Chen, and S. T. Wu, “Device simulation of liquid crystal polarization gratings,” *Opt. Express* 27, 18102-18112 (2019).
- [35] Y. H. Lee, Z. He, and S. T. Wu, “Optical properties of reflective liquid crystal polarization volume gratings,” *J. Opt. Soc. America B*, 36, D9-D12 (2019).
- [36] K. Yin, T. Zhan, J. Xiong, Z. He, and S. T. Wu, “Polarization Volume Gratings for Near-eye Displays and Novel Photonic Devices,” *Crystals* 10, 561 (2020).
- [37] D. W. Berreman, “Solid surface shape and the alignment of an adjacent nematic liquid crystal,” *Phys. Rev. Lett.* 28, 1683–1686 (1972).

- [38] J. Kim, Y. Li, M. N. Miskiewicz, C. Oh, M. W. Kudenov, and M. J. Escuti, “Fabrication of ideal geometric-phase holograms with arbitrary wavefronts,” *Optica* 2, 958–964 (2015).
- [39] V. Chigrinov, A. Kudreyko, and Q. Guo, “Patterned Photoalignment in Thin Films: Physics and Applications,” *Crystals* 11, 84 (2021).
- [40] V. Chigrinov, A. Muravski, H. S. Kwok, H. Takada, H. Akiyama, and H. Takatsu, “Anchoring properties of photoaligned azo-dye materials,” *Phys. Rev. E* 68, 061702. (2003).
- [41] M. C. Tseng, O. Yaroshchuk, T. Bidna, A. K. Srivastava, V. Chigrinov, and H. S. Kwok, “Strengthening of liquid crystal photoalignment on azo dye films: Passivation by reactive mesogens,” *RSC Adv.* 6, 48181–48188 (2016).
- [42] J. Wang, C. McGinty, R. Reich, V. Finnemeyer, H. Clark, S. Berry, P. Bos, “Process for a reactive monomer alignment layer for liquid crystals formed on an azodye sublayer,” *Materials* 11, 1195 (2018).
- [43] J. Wang, C. McGinty, J. West, D. Bryant, V. Finnemeyer, R. Reich, S. Berry, H. Clark, O. Yaroshchuk, and P. Bos, “Effects of humidity and surface on photoalignment of brilliant yellow,” *Liq. Cryst.* 44, 863–872 (2017).
- [44] E. Ouskova, R. Vergara, J. Hwang, D. Roberts, D. M. Steeves, B. R. Kimball, N. Tabiryan, “Dual-function reversible/irreversible photoalignment material,” *J. Mol. Liq.* 267, 205–211 (2018).
- [45] C. Decker and K. Moussa, “Real-time kinetic study of laser-induced polymerization,” *Macromolecules* 22, 4455–4462 (1989).

- [46] S. J. Bryant, C. R. Nuttelman, and K. S. Anseth, “Cytocompatibility of UV and visible light photoinitiating systems on cultured NIH/3T3 fibroblasts in vitro,” *J. Biomater. Sci. Polym. Ed.* 11, 439–457 (2000).
- [47] D. K. Yang and S. T. Wu, *Fundamentals of Liquid Crystal Devices, 2nd ed.* (Wiley, 2014).
- [48] M. F. Schiekkel and K. Fahrenschon, “Deformation of Nematic Liquid Crystals with Vertical Orientation in Electrical Fields,” *Appl. Phys. Lett.* 19, 391–393 (1971).
- [49] K. Gao, C. McGinty, H. Payson, S. Berry, J. Vornehm, V. Finnemeyer, B. Roberts, and P. Bos, “High-efficiency large-angle Pancharatnam phase deflector based on dual-twist design,” *Opt. Express* 25, 6283–6293 (2017).
- [50] S. D. Kakichashvili, “Method for phase polarization recording of holograms,” *Sov. J. Quantum Electron.* 4, 795–798 (1974).
- [51] G. P. Crawford, J. N. Eakin, M. D. Radcliffe, A. Callan-Jones, and R. A. Pelcovits, “Liquid-crystal diffraction gratings using polarization holography alignment techniques,” *J. Appl. Phys.* 98, 123102 (2005).
- [52] P. Chen, B. Y. Wei, W. Hu, and Y. Q. Lu, “Liquid-Crystal-Mediated Geometric Phase: From Transmissive to Broadband Reflective Planar Optics,” *Adv. Mater.* 31, 1903665 (2019).
- [53] L. De Sio, D. E. Roberts, Z. Liao, S. Nersisyan, O. Uskova, L. Wickboldt, N. Tabiryan, D. M. Steeves, and B. R. Kimball, “Digital polarization holography advancing geometrical phase optics,” *Opt. Express* 24, 18297–18306 (2016).

- [54] H. Wu, W. Hu, H. C. Hu, X. W. Lin, G. Zhu, J. W. Choi, V. Chigrinov, and Y. Q. Lu, “Arbitrary photo-patterning in liquid crystal alignments using DMD based lithography system,” *Opt. Express* 20, 16684–16689 (2012).
- [55] W. R. Sherman and A. B. Craig, *Understanding virtual reality*. (San Francisco, CA: Morgan Kauffman, 2003).
- [56] A. Maimone and J. Wang, “Holographic optics for thin and lightweight virtual reality,” *ACM Trans. Graph.* 39, 67 (2020).
- [57] B. Bastani, E. Turner, C. Vieri, H. Jiang, B. Funt, and N. Balram, “Foveated pipeline for AR/VR head-mounted displays,” *Inf. Disp.* 33, 14–19 (2017).
- [58] G. Tan, Y. H. Lee, T. Zhan, J. Yang, S. Liu, D. F. Zhao, and S. T. Wu, “Foveated imaging for near-eye displays,” *Opt. Express* 26, 25076-25085 (2018).
- [59] C. Yoo, J. Xiong, S. Moon, D. Yoo, C-K. Lee, S. T. Wu, and B. Lee, “Foveated display system based on a doublet geometric phase lens,” *Opt. Express* 28, 23690-23702 (2020).
- [60] J. Kim, Y. Jeong, M. Stengel, K. Akşit, R. Albert, B. Boudaoud, T. Greer, J. Kim, W. Lopes, Z. Majercik, and P. Shirley, “Foveated AR: dynamically-foveated augmented reality display,” *ACM Trans. Graph.* 38, 1-5 (2019).
- [61] K. Akşit, P. Chakravarthula, K. Rathinavel, Y. Jeong, R. Albert, H. Fuchs, and D. Luebke, “Manufacturing application-driven foveated near-eye displays,” *IEEE Trans. Vis. Comput. Graph.* 25, 1928-1939 (2019).
- [62] S. Lee, M. Wang, G. Li, L. Lu, Y. Sulai, C. Jang, and B. “Silverstein. Foveated near-eye display for mixed reality using liquid crystal photonics,” *Sci. Rep.* 10, 1-1 (2020).

- [63] P. K. Brown and G. Wald, "Visual pigments of rods and cones in a human retina," *Science* 144, 45-52 (1964).
- [64] G. Tan, T. Zhan, Y. H. Lee, J. Xiong, and S. T. Wu, "Polarization-multiplexed multiplane display," *Opt. Lett.* 43, 5651-5654 (2018).
- [65] J. Zou, E. L. Hsiang, T. Zhan, K. Yin, Z. He, and S. T. Wu, "High Dynamic Range Head-up Display," *Opt. Express* 28, 24298-24307 (2020).
- [66] H. M. Knight, P. R. Gajendragadkar, and A. Bokhari, "Wearable technology: using Google Glass as a teaching tool," *Case Reports*, bcr2014208768 (2015).
- [67] O. M. Tepper, H. L. Rudy, A. Lefkowitz, K. A. Weimer, S. M. Marks, C. S. Stern, and E. S. Garfein, "Mixed reality with HoloLens: where virtual reality meets augmented reality in the operating room," *Plastic and reconstructive surgery* 140, 1066-1070 (2017).
- [68] F. Bruder, T. Fäcke, R. Hagen, D. Hönel, E. Orselli, C. Rewitz, T. Rölle, and G. Walze, "Diffractive optics with high Bragg selectivity: volume holographic optical elements in Bayfol® HX photopolymer film," *Proc. SPIE* 9626, 96260T (2015).
- [69] R. L. Sutherland, L. V. Natarajan, V. P. Tondiglia, and T. J. Bunning, "Bragg gratings in an acrylate polymer consisting of periodic polymer-dispersed liquid-crystal planes," *Chem. Mater.* 5, 1533-1538 (1993).
- [70] Y. J. Liu and X. W. Sun, "Holographic polymer-dispersed liquid crystals materials, formation, and applications," *Adv. Optoelectron.* 2008, 684349 (2008).
- [71] T. Levola, "Novel diffractive optical components for near to eye displays," *SID Int. Symp. Digest Tech. Papers* 37, 64-67 (2006).



- [72] J. Kobashi, Y. Mohri, H. Yoshida, and M. Ozaki, “Circularly-polarized, large-angle reflective deflectors based on periodically patterned cholesteric liquid crystals,” *Opt. Data Process. Storage* 3, 61–66 (2017).
- [73] D. J. Broer, J. Lub, and G. N. Mol, “Wide-band reflective polarizers from cholesteric polymer networks with a pitch gradient,” *Nature* 378, 467–469 (1995).
- [74] D. Katsis, D. U. Kim, H. P. Chen, L. J. Rothberg, S. H. Chen, and T. Tsutsui, “Circularly polarized photoluminescence from gradient-pitch chiral-nematic films,” *Chem. Mater.* 13, 643–647 (2001).
- [75] Q. Hong, T. X. Wu, and S. T. Wu, “Optical wave propagation in a cholesteric liquid crystal using the finite element method,” *Liq. Cryst.* 30, 367–375 (2003).
- [76] K. Yin, H. Y. Lin, and S. T. Wu, “Chirped polarization volume grating with ultra-wide angular bandwidth and high efficiency for see-through near-eye displays,” *Opt. Express* 27(24), 35895-35902 (2019).
- [77] X. Xiang, J. Kim, and M. J. Escuti, “Bragg polarization gratings for wide angular bandwidth and high efficiency at steep deflection angles,” *Sci. Rep.* 8, 7202 (2018).
- [78] K. Yin, H. Y. Lin, and S. T. Wu, “Chirped polarization volume grating for wide FOV and high efficiency waveguide-based AR displays,” *J. Soc. Inf. Disp.* 28, 368-374 (2020).
- [79] K. Yin, Y. H. Lee, Z. He, and S. T. Wu, “Stretchable, flexible, and adherable polarization volume grating film for waveguide-based augmented reality displays,” *J. Soc. Inf. Disp.* 27, 232-237 (2019).
- [80] B. Kress, “Optical waveguide combiners for AR headsets: features and limitations,” *Proc. SPIE* 11062, 17 (2019).

- [81] Y. Weng, Y. Zhang, J. Cui, A. Liu, Z. Shen, X. Li, and B. Wang, "Liquid-crystal-based polarization volume grating applied for full-color waveguide displays," *Opt. Lett.* 43(23), 5773–5776 (2018).
- [82] A. Liu, Y. Zhang, Y. Weng, Z. Shen, and B. Wang, "Diffraction efficiency distribution of output grating in holographic waveguide display system," *IEEE Photonics Journal* 10, 1-10 (2018).
- [83] H. Huang and H. Hua, "High-performance integral-imaging-based light field augmented reality display using freeform optics," *Opt. Express* 26, 17578–17590 (2018).
- [84] J. Rolland and H. Hua, "Head-mounted display systems," *Encyclopedia of Optical Engineering* 2, 1-14 (2005).
- [85] H. Hua and J. Bahram, "A 3D integral imaging optical see-through head-mounted display," *Opt. Express* 22, 13484-13491 (2014).
- [86] O. Cakmakci and J. Rolland, "Design and fabrication of a dual-element off-axis near-eye optical magnifier," *Opt. Lett.* 32, 1363–1365 (2007).
- [87] H. Hua, X. Hu, and C. Gao, "A high-resolution optical see-through head-mounted display with eyetracking capability," *Opt. Express* 21, 30993–30998 (2013).
- [88] S. Lee, B. Lee, J. Cho, C. Jang, J. Kim, and B. Lee, "Analysis and implementation of hologram lenses for see-through head-mounted display," *IEEE Photonics Technol. Lett.* 29(1), 82–85 (2017).
- [89] J. Xiong, Y. Li, K. Li, and S. T. Wu, "Aberration-free pupil steerable Maxwellian display for augmented reality with cholesteric liquid crystal holographic lenses," *Opt. Lett.* 46, 1760-1763 (2021).

- [90] C. Chang, K. Bang, G. Wetzstein, B. Lee, and L. Gao, "Toward the next-generation VR/AR optics: a review of holographic near-eye displays from a human-centric perspective," *Optica* 7, 1563 (2020).
- [91] K. Yin, Z. He, K. Li, and S. T. Wu, "Doubling the FOV of AR displays with a liquid crystal polarization-dependent combiner," *Opt. Express* 29, 11512-11519 (2021).
- [92] Y. H. Lee, T. Zhan, and S. T. Wu, "Prospects and challenges in augmented reality displays," *Virtual Reality & Intelligent Hardware* 1, 10–20 (2019).
- [93] H. Peng, D. Cheng, J. Han, C. Xu, W. Song, L. Ha, J. Yang, Q. Hu, and Y. Wang, "Design and fabrication of a holographic head-up display with asymmetric field of view," *Appl. Opt.* 53, H177–H185 (2014).
- [94] R. L. Fisher, "Design methods for a holographic head-up display curved combiner," *Opt. Eng.* 28, 616–621 (1989).
- [95] J. P. Rolland, "Wide-angle, off-axis, see-through head-mounted display," *Opt. Eng.* 39, 1760–1767 (2000).
- [96] Y. Amitai, A. A. Friesem, and V. Weiss, "Designing holographic lenses with different recording and readout wavelengths," *J. Opt. Soc. Am. A* 7, 80-86 (1990).
- [97] Z. Shi, W. T. Chen, and F. Capasso, "Wide field-of-view waveguide displays enabled by polarization-dependent metagratings," *Proc. SPIE* 10676, 1067615 (2018).
- [98] C. Yoo, K. Bang, M. Chae, and B. Lee, "Extended-viewing-angle waveguide near-eye display with a polarization-dependent steering combiner," *Opt. Lett.* 45, 2870–2873 (2020).
- [99] K. Yin, Z. He, K. Li, and S. T. Wu, "Novel polarization-dependent combiner for wide field-of-view glass-like near-eye displays," *J. Soc. Inf. Display* 29, 311-317 (2021).

- [100] R. A. Flasck, "The Critical Role of Optical Interference Coatings in High Brightness - Etendue Limited Systems Such as HDTV Projectors," Optical Interference Coatings, OSA Technical Digest (CD), ThC5 (2007).
- [101] N. Abu-Ageel and D. Aslam, "Laser-Driven Visible Solid-State Light Source for Etendue-Limited Applications," *J. Display Technol.* 10, 700-703 (2014).
- [102] P. P. Manousiadis, S. Rajbhandari, R. Mulyawan, D. A. Vithanage, H. Chun, G. Faulkner, D. C. O'Brien, G. A. Turnbull, S. Collins, and I. D. W. Samuel, "Wide field-of-view fluorescent antenna for visible light communications beyond the étendue limit," *Optica* 3, 702-706 (2016).
- [103] P. Patel-Schneider, "System description: DLP," International Conference on Automated Deduction. Springer, Berlin, Heidelberg, 297-301 (2000).
- [104] H. Zou, A. Schleicher, and J. Dean. "58.1: Single-panel LCOS color projector with LED light sources," *SID Symp. Digest.* 36, 1698-1701 (2005).
- [105] J. Zou, Q. Yang, E. L. Hsiang, H. Ooishi, Z. Yang, K. Yoshidaya, and S. T. Wu, "Fast-Response Liquid Crystal for Spatial Light Modulator and LiDAR Applications," *Crystals* 11, 93 (2021).
- [106] S. T. Wu and C. S. Wu, "Mixed-mode twisted nematic liquid crystal cells for reflective displays," *Appl. Phys. Lett.* 68, 1455-1457 (1996).
- [107] C. H. Gooch and H. A. Tarry, "The optical properties of twisted nematic liquid crystal structures with twist angles  $\leq 90$  degrees," *J. Phys. D: Appl. Phys.* 8, 1575(1975).
- [108] M. Schadt and W. Helfrich, "Voltage-dependent optical activity of a twisted nematic liquid crystal," *Appl. Phys. Lett.* 18, 127-128 (1971).

[109] C. Parkhurst and R. L. Feller, "Who invented the color wheel?" *Color Research & Application*, 7, 217-230 (1982).